Plasma-catalytic ammonia synthesis : packed catalysts act as plasma modifiers

Plasma-catalytic ammonia synthesis: Packed catalysts act as plasma modifiers

Callie Ndayirinde[a], Yury Gorbanev[a], Radu-George Ciocarlan[b], Alessandro Smets[a,b], Evgenii Vlasov[c], Robin De Meyer[a,c], Sara Bals[c], Pegie Cool[b], Annemie Bogaerts[a]

[a]Research group PLASMANT, Department of Chemistry, University of Antwerp, Universiteitsplein 1, B-2610 Wilrijk-Antwerp, Belgium.

[b]Research group LADCA, Department of Chemistry, University of Antwerp, Universiteitsplein 1, B-2610 Wilrijk-Antwerp, Belgium.

[c]Research group EMAT, Department of Physics, University of Antwerp, Groenenborgerlaan 171, 2020 Antwerp, Belgium

Keywords: Plasma catalysis, N_2 fixation, ammonia production, non-thermal plasma, Cobalt-based catalysts

Abstract

We studied the plasma-catalytic production of NH_3 from H_2 and N_2 in a dielectric barrier discharge plasma reactor using five different Co-based catalysts supported on Al_2O_3, namely Co/Al_2O_3, $CoCe/Al_2O_3$, $CoLa/Al_2O_3$, $CoCeLa/Al_2O_3$ and $CoCeMg/Al_2O_3$. The catalysts were characterized via several techniques, including SEM-EDX, and their performance was compared. The best performing catalyst was

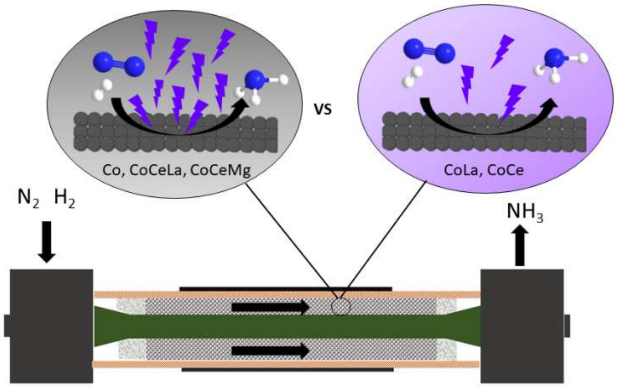

found to be $CoLa/Al_2O_3$, but the differences in NH_3 concentration, energy consumption and production rate between the different catalysts were limited under the same conditions (i.e. feed gas, flow rate and ratio, and applied power). At the same time, the plasma properties, such as the plasma power and current profile, varied significantly depending on the catalyst. Taken together, these findings suggest that in the production of NH_3 by plasma catalysis, our catalysts act as plasma modifiers, i.e., they change the discharge properties and hence the gas phase plasma chemistry. Importantly, this effect dominates over the direct catalytic effect (as e.g. in thermal catalysis) defined by the chemistry on the catalyst surface.

1. Introduction

The steep increase in the world population results in a growing global demand for a variety of necessities, especially food.[1] To accommodate this growing food demand, fertilizers are widely used to increase the global food production.[2] Ammonia (NH_3) based fertilizers are among the most commonly used fertilizers in the agricultural sector. Besides agricultural purposes, NH_3 is also gaining attention as a hydrogen carrier and energy storage chemical.[3-5]

At present, NH_3 is mainly synthesized via the Haber Bosch (HB) process, which produces over 150 million tons of NH_3 annually.[6-8] However, the production of NH_3 via the HB process is a highly energy-intensive method: it consumes up to 2% of the global energy supply, and requires extremely high pressures (100-450 bar) and high temperatures (400°C - 500°C) to obtain a significant yield and to make the process cost-effective.[6] To enable these conditions, the HB process uses fossil fuel (natural gas, oil and coal) as feedstock, and as a result, ca. 1.9 tons of CO_2 is generated per ton of NH_3 produced.[6, 8, 9]

Consequently, alternative strategies[10] for a green NH_3 production are widely investigated.[9, 11] Among other techniques, non-thermal plasma (NTP) catalytic NH_3 synthesis has recently gained a lot of attention as a potential sustainable, green alternative for the HB process.

NTPs are characterized by high-energy electrons (10^4-10^5 K) that can cause non-thermal activation of molecules, while the gas temperature remains between 300 K - 1000 K.[12, 13] As a result, reactions can take place at lower pressures and temperatures compared to thermal catalysis. However, NTPs contain a wide range of highly reactive species, making it difficult to obtain a single product at a high yield and with a high selectivity.[14] Yet, combining NTPs with catalysts can lead to a synergistic effect with the efficiency of the combined system surpassing that of the

individual parts.[14-16] Further, NTPs allow for quick on/off operation making the technology compatible with the fluctuating renewable energy sources such as wind energy and solar power, enabling a novel green way to synthesize NH_3.[13, 17]

Dielectric barrier discharge (DBD) plasma reactors are often chosen for the plasma-catalytic synthesis of NH_3 because it provides good contact between the plasma and the catalysts, and the plasma operates at ambient conditions.[16] In 2018, Mehta et al.[18] designed a density functional theory based microkinetic model, suggesting that vibrationally excited N_2 enhances the N_2 dissociation rate and therefore the NH_3 synthesis rate. Consequently, the top of the classic "volcano" plot, or in other words - the optimal metal catalyst, shifts from Fe and Ru in thermal catalysis, towards weaker binding metals, such as Co and Ni, in plasma catalysis.[18] Various studies have been reported in which the plasma-catalytic synthesis of NH_3 has been investigated over different transition metal catalysts, such as Ni, Fe, Cu, Ru and Co.[3, 4, 18-23] Several transition metal catalysts employed in these studies are supported on Al_2O_3[24], but MgO, SiO_2 and activated carbon are also often used.[5, 23-27] From the aforementioned studies, different catalysts were deemed to be optimal for the plasma-catalytic NH_3 synthesis. One of the reasons for these discrepancies in results is that not only the catalyst changes from one study to another, but also the plasma and reaction conditions are different, rendering the direct comparison difficult.

Furthermore, our recent experimental[21] and computational[28] works showed that the nature of the metal in monometallic catalysts, while having an impact on the catalytic efficiency, does not produce differences large enough to yield a "volcano" plot. The same behaviour was also experimentally observed by other authors.[3, 18, 29] A brief summary of the reported advances in the state-of-the-art on plasma-catalytic NH_3 synthesis in the past two decades is given in Table S1 in Supporting Information (SI).

Even though quite some advances have been made in the field of plasma-catalytic synthesis of NH_3, many fundamental questions remain open. For example, there is no clear understanding on how (and whether) the knowledge from thermal catalysis translates into plasma catalysis. The aforementioned shift in the "volcano" plot is a good example of inapplicability of a direct translation. Furthermore, the effect of the active metals on the NH_3 production rate and the interaction or synergy between the catalysts and plasma remain unclear.

Previous research in plasma catalysis showed the higher efficiency of Co compared to other catalysts.[18, 20, 21] At the same time, bi- and tri-metallic Co-based catalysts with added Ce and Ba,

were shown to be efficient for NH_3 synthesis, in thermal catalysis, under milder conditions than the industry-dominating HB process.[30] To elucidate whether a similar effect is present in plasma catalysis, we investigated in this work the effect of combining Co with other metals in plasma catalysis. For this, Ce with and without other metals was added to Co-based alumina-supported catalysts.

Specifically, we studied the effect of five different catalysts, namely 20 wt% Co/Al_2O_3, $CoCe/Al_2O_3$, $CoCeMg/Al_2O_3$, $CoCeLa/Al_2O_3$ and cerium-free $CoLa/Al_2O_3$, on the formation of NH_3 from N_2 and H_2 in a DBD plasma reactor. In our previous investigation[21], we showed that 10 wt% Al_2O_3-supported catalysts contained metal nanoparticles on the porous alumina, as anticipated. The coverage of the support surface, however, ranged between 7% and 15% of the total catalyst surface area.[21] In continuous flow plasma reactors, the interaction of the gas phase species with the catalytic surface could be a limiting factor. Therefore, in the present work we increased the metal loading so that a larger fraction of the catalyst bead surface is covered with active metals.

The effect of the metal composition of the catalysts on their plasma-catalytic performance for NH_3 synthesis was assessed by evaluating the production rate (PR) and the NH_3 concentration in the plasma reactor exhaust, as well as the energy consumption (EC) of the process. Moreover, the performance of the bi- and tri-metallic catalysts was compared for this reaction with Co/Al_2O_3, pure Al_2O_3 and plasma alone. Additionally, in order to find the optimal operational conditions, the plasma-catalytic experiments were carried out for three different H_2:N_2 ratios (stoichiometric 3:1, 1:1 and 1:3) at two different total feed gas flow rates (100 mLn/min and 200 mLn/min – normal millilitres per minute, referred to as "mL/min" in the rest of the paper for simplicity). In addition, multiple characterization techniques were applied to determine the differences in the physico-chemical properties of the catalysts. Importantly, we also monitored the properties of the discharge to evaluate the effect of the catalyst on plasma – a phenomenon that is often overlooked in plasma-catalytic research.

2. Material and methods

2.1 Catalyst preparation

The metal catalysts were prepared via wet impregnation of γ-Al_2O_3 beads (1.8 mm diameter), obtained from Sasol. The following metal nitrate hydrates were used as precursors (all purchased from Sigma-Aldrich): $Ce(NO_3)_3.6H_2O$ (99%), $Mg(NO_3)_2.6H_2O$ (99%), $Co(NO_3)_2.6H_2O$ (98%)

and $La(NO_3)_3.6H_2O$ (p.a.). The quantities of the precursor solutions were calculated so that the amount of the adsorbed metal nitrates would correspond to a 20 wt% loading of the respective reduced metals.

An aqueous solution containing one, two or three metal precursors, i.e.: $Ce(NO_3)_3.6H_2O$ (99%), $Mg(NO_3)_2.6H_2O$ (99%), $Co(NO_3)_2.6H_2O$ (98%) and $La(NO_3)_3.6H_2O$ (p.a.), was prepared for the wet impregnation of the γ-Al_2O_3 beads for the synthesis of the mono-, bi- and trimetallic catalysts, respectively. The volume of solution (0.69 mL per 1 g of beads) was found empirically as the maximal volume which can be absorbed by the beads. The solution was added to the beads and stirred manually until the beads were homogeneously coloured. The coloured beads were dried overnight at room temperature (RT) in air. Next, the beads were dried in an oven at 120 °C for 24 h. At this point, a metal loading of 10 wt% on the γ-Al_2O_3 beads was obtained. Afterwards, the wet impregnation process was repeated with the dried spheres to reach a total loading of 20 wt%. The impregnated Al_2O_3 beads were again dried overnight at RT in air. Finally, the beads were dried in an oven at 120 °C for 24 h, followed by a calcination at 600 °C under atmospheric air for 6 h, at a ramp of 2 °C/min. Prior to plasma experiments, the catalysts were reduced in an H_2 plasma for 8 h.

2.2 Reactor setup

The DBD reactor consists of an inner ground electrode (stainless steel, 8.0 mm diameter) which is placed in the centre of a hollow ceramic cylinder, illustrated in Figure 1. Mass flow controllers (Bronkhorst F-201CV), that are connected to an H_2 gas cylinder (99.999%, Air Liquide) and an N_2 gas cylinder (99.999%, Praxair) introduce the feed gasses H_2 and N_2 into the DBD reactor. The ceramic cylinder functions as a dielectric barrier and has an inner diameter of 17.4 mm and a thickness of 2.4 mm. As a result, a gap of ca. 4.7 mm exists between the ceramic and the inner electrode. A stainless steel mesh electrode (165.0 mm length, ca. 1 mm thickness) is wrapped around the ceramic cylinder, held in place with Kapton tape, and is powered by high voltage. The catalytic materials (Al_2O_3 beads impregnated with catalytically active metals) are introduced inside this gap until the volume inside the ceramic tube corresponding to the outer electrode length is filled with them. When measured with a volumetric cylinder, the total occupied volume of beads was ca. 30 mL and ca. 16 g in each experiment. The beads are held in place on both sides by glass wool.

The discharge is sustained by a power supply unit (PSU) (AFS GmbH, G10S-V2x), connected to a transformer. The PSU is used at a set power of 100 W (total PSU power) and a frequency of 23.5 kHz for all experiments. The power adsorbed by the plasma, often referred to as plasma power or deposited power, is estimated from the charge-voltage (Q-U) Lissajous figures by calculating the area enclosed under the curves.[31] The plasma power is often lower than the set PSU power but maximising the power consumed by the plasma is out of the scope of our work.[32] In this work we focus on using a set PSU power as this is more addressed in industry applications than the plasma power.

In addition, the electrical properties of the plasma discharge setup are monitored with an oscilloscope (Pico Technology, PicoScope 6402D) by means of a high voltage probe (Tektronix P6015A) and a current monitor (Pearson Electronics, Model 4100).

The NH_3 concentration in the gas outlet from the DBD reactor was measured by non-dispersive infrared (NDIR) (Emerson, RosemountTM X-stream Enhanced XEGP Continuous Gas Analyzer). Prior to the measurements, the NDIR was calibrated with 4.89 vol% NH_3 in He, purchased from Praxair. The calibration curve is shown in SI section S1.

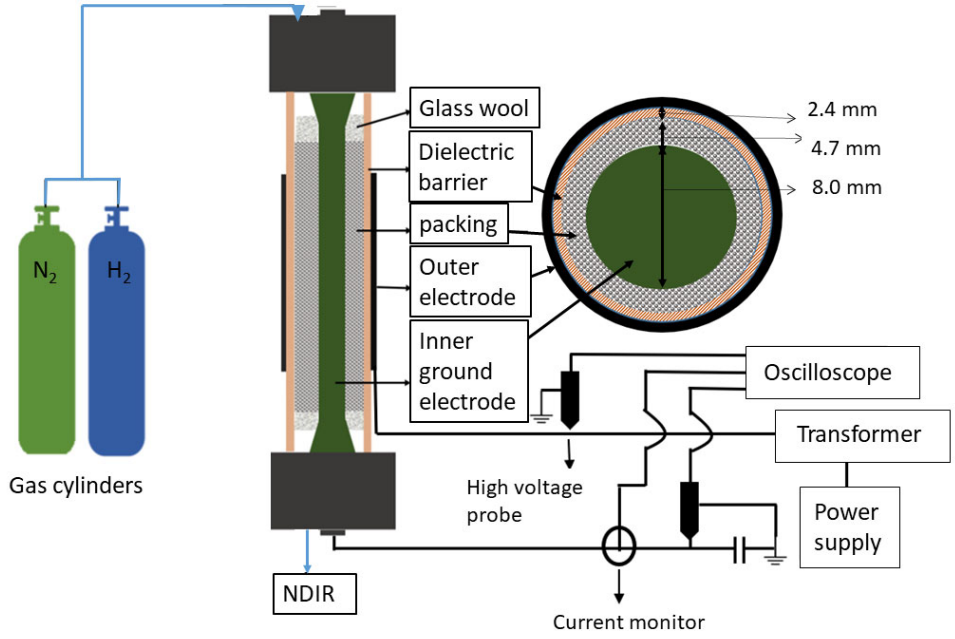

Figure 1: Schematic representation of the DBD reactor used for plasma-catalytic NH_3 synthesis.

2.3 Catalyst characterization

The structural properties of the catalysts were investigated using Raman spectroscopy and X-Ray powder diffraction (XRPD). The XRPD measurements were executed with a Bruker D8 ADVANCE Eco X-ray diffractometer equipped with an X-ray source of CuKα radiation λ= 0.15406 nm. The analysis was carried out over a 2θ range of 10 to 80 degrees in steps of 0.04 ° and 4 s per step. All catalyst beads were crushed into a homogeneous powder with a mortar and pestle prior to the analysis.

The Raman spectra were recorded on a Horiba XploRA Plus Raman spectrometer equipped with a diode-pumped solid-state laser of 532 nm and a power of 25 mW. The samples were measured with an acquisition time of 10 s, 10 accumulations and in a spectral range of 100-2000 cm^{-1}. The spectra were acquired in two different spots on two different beads, in order to verify the homogeneity of the catalysts.

The metal loading and distribution throughout the bead were investigated using scanning electron microscopy and energy dispersive X-ray spectroscopy (SEM-EDX). The analysis was performed using the FEI Quanta FEG 250 ESEM, operated at 20 kV and under high vacuum. Before analysis, all the catalyst beads were embedded in a two-component epoxy resin (EPO-TEK 353ND-T4), which was hardened and cross-sectioned via polishing. After polishing, the samples were coated with 10 nm carbon to prevent charging during further analysis. The analysis was performed on two different beads, in order to verify the homogeneity of the catalysts. SEM-EDX maps were acquired using an X-Max (Oxford Instruments) silicon drift detector. Data acquisition and quantification were performed using INCA software. The maps were acquired from a rectangular area with a size of 256x170 pixels. During the post-processing stage, a MATLAB script was used to retrieve the radial distribution of the metal content over the acquired map after detection of the center of the beads and their edges; as illustrated in SI in Figure S3F.

The pore volume and specific surface area were investigated using N_2 physisorption. The N_2 sorption analysis was carried out on a Quantachrome Quadrasorb SI automated gas sorption system. First the samples were degassed under vacuum for 16 h at a temperature of 200 °C. The actual measurements were executed at the temperature of liquid N_2 (-196 °C) and N_2 was used as an adsorbate.

3. Calculation

The energy consumption (EC) in MJ per mol NH_3 produced, production rate (PR) of NH_3 in mg/h and the specific energy input (SEI) were calculated as shown below in formulae F1-F4.

In this study the energy consumption (EC) was calculated in the following manner, to account for the contraction of gas due to the stoichiometry of NH_3 formation:

$$\text{EC (MJ/mol)} = \frac{\mathrm{P(W)}}{\frac{\mathrm{F_{NH_3}}\left(\frac{\mathrm{mL}}{\mathrm{min}}\right)}{\mathrm{V_m}\left(\frac{\mathrm{L}}{\mathrm{mol}}\right)\cdot 10^3\left(\frac{\mathrm{mL}}{\mathrm{L}}\right)\cdot 60\left(\frac{\mathrm{s}}{\mathrm{min}}\right)}} \cdot 10^{-6}\left(\frac{\mathrm{MJ}}{\mathrm{J}}\right) \quad \text{(F1)}$$

$$\text{and } F_{NH_3}\text{(mL/min)} = \frac{\left[\left(\mathrm{F_{H_2}}\left(\frac{\mathrm{mL}}{\mathrm{min}}\right) + \mathrm{F_{N_2}}\left(\frac{\mathrm{mL}}{\mathrm{min}}\right)\right)\cdot\frac{\mathrm{C_{NH_3(vol\%)}}}{100}\right]}{\left[1+\frac{\mathrm{C_{NH_3(vol\%)}}}{100}\right]} \quad \text{(F2)}$$

With P = power deposited into plasma,

Vm= molar volume of an ideal gas at normal conditions (i.e. 22.4 L/mol at 1 atm and 273 Kelvin).[33]

The production rate was calculated in the following manner:

$$\text{Production rate (mg/h)} = \frac{\mathrm{F_{NH_3}}\left(\frac{\mathrm{mL}}{\mathrm{min}}\right)}{\mathrm{V_m}\left(\frac{\mathrm{L}}{\mathrm{mol}}\right)} \cdot 10^{-3}\left(\frac{\mathrm{L}}{\mathrm{mL}}\right) \cdot 60\left(\frac{\mathrm{min}}{\mathrm{h}}\right) \cdot \mathrm{M_{NH_3}}\left(\frac{\mathrm{g}}{\mathrm{mol}}\right) \cdot 10^3\left(\frac{\mathrm{mg}}{\mathrm{g}}\right) \quad \text{(F3)}$$

The specific energy input (SEI) is calculated in the following manner:

$$\mathrm{SEI}\left(\frac{J}{L}\right) = \frac{\mathrm{P(W)}*60\left(\frac{\mathrm{s}}{\mathrm{min}}\right)}{\mathrm{F_{gas}}\left(\frac{\mathrm{L}}{\mathrm{min}}\right)} \quad \text{(F4)}$$

Lastly, the cell capacitance (C_{cell}) is obtained by taking the maximum observed slope of the "discharge off" phase of the Lissajous figure. While the effective capacitance (C_{eff}) is calculated by taking the maximum observed slope of the "plasma on" phase of the Lissajous figure.[31]

4. Results and discussion

4.1. Catalyst characterization

4.1.1. XRPD

XRPD and Raman spectroscopic analyses, shown in SI section S2, showed that the freshly prepared unreduced catalysts were comprised of the respective metal oxides. The XRPD patterns of the catalysts are illustrated in Figure 2. All samples exhibit diffraction maxima at 2θ = 19°, 31°, 37°, 39°, 45°, 57°, 60°, 65°, 74° and 77° which can be assigned to (111), (220), (311), (222), (400), (422), (511), (440), (620) and (533) crystallographic planes of cubic Co_3O_4[34] and cubic $CoAl_2O_4$[35]

since these compounds have similar spinel cubic crystallographic structure (Fd-3m).[36] Furthermore, these crystallographic planes can also be assigned to $MgAl_2O_4$, which is also characterized by the Fd-3m crystallographic structure, in the case of $CoCeMg/Al_2O_3$.[37] In addition, all samples also show diffraction maxima at 2θ = 19°, 30°, 37°, 46° and 67°, which correspond to the reflections of the (111), (220), (311), (400) and (440) planes of cubic γ-Al_2O_3, the support of the catalysts.[38, 39] Besides, $CoCe/Al_2O_3$, $CoCeMg/Al_2O_3$ and $CoCeLa/Al_2O_3$ present diffraction maxima at 2θ = 29°, 33°, 48°, 57°, 70°, 77° and 79°, which can be attributed to (111), (200), (220), (311), (400), (331) and (420) planes of cubic fluorite CeO_2.[40, 41]

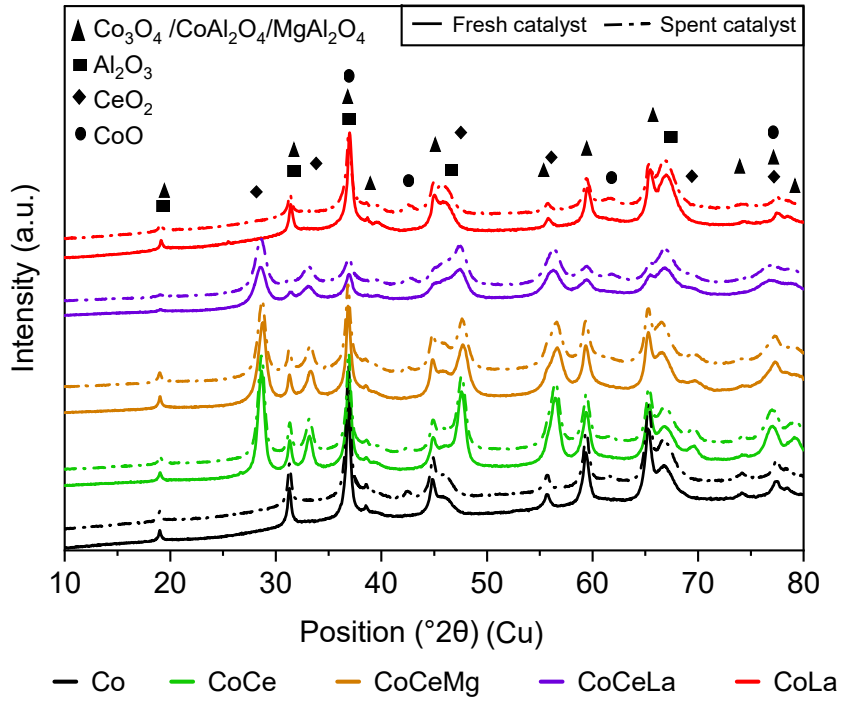

Figure 2: The XRPD patterns of fresh and spent Co/Al_2O_3, $CoCe/Al_2O_3$, $CoCeMg/Al_2O_3$, $CoCeLa/Al_2O_3$ and $CoLa/Al_2O_3$ catalysts.

In addition, the spent catalysts show additional diffraction maxima at 2θ = 37°, 42°, 62° and 78° which corresponds to (111), (200), (220) and (222) planes of face centered cubic (fcc) CoO.[42] The presence of CoO in the X-ray diffractograms proves that the H_2 plasma indeed reduces the catalysts. Yet, no metallic Co, Ce, Mg or La was observed because reduction by an H_2 plasma mainly reduces the outer surface of the beads and prior to the XRD analysis, the beads were crushed. However, this reduction method is sufficient for NTP experiments that employ

mesoporous catalysts since the plasma does not ignite inside the pores[43] and the gas temperature (<120 °C)[21] is too low for thermal-catalytic conversion to occur inside the pores.[44]

No phase containing lanthanum is detected for the lanthanum-containing samples, indicating that lanthanum oxide is amorphous or highly dispersed, which could result in crystallites with sizes below the detection limit, or form spinel-like structures with the characteristic features overlapping the other spinel structures. However, the presence of these metals can be confirmed by SEM-EDX.

4.1.2 SEM-EDX

During the synthesis, a total metal loading of 20 wt% was anticipated for all catalysts, with a 3:1 (Co:M1) molar ratio for the bimetallic catalysts, a 2:1:1 (Co:Ce:La) molar ratio for $CoCeLa/Al_2O_3$ and a 3:1:3 (Co:Ce:Mg) molar ratio for $CoCeMg/Al_2O_3$. The EDX maps of the cross-section samples were acquired with the SEM at an acceleration voltage of 20 kV. The obtained metal content and molar ratio of the spent catalysts is shown in Table 1. Generally, the metal loading and molar ratios are in good agreement with the values calculated in preparation. The minor discrepancies between expected and measured metal loading and molar ratio of metals are likely due to SEM-EDX being an inherently local analysis, and a not perfectly uniform distribution of metal over the total number of catalyst beads. The SEM images, the radial distribution of metal content over catalytic beads and the EDX maps are shown in SI in section S3.

Table 1: The metal loading and molar ratio of the spent Al_2O_3-supported catalysts.

Catalyst	**Co (wt%)**	**Ce (wt%)**	**La (wt%)**	**Mg (wt%)**	**Total metal loading (wt%)**	**Molar ratio (Co:M1:M2)**
Co/Al_2O_3	16.9 ± 1.6	-	-	-	16.9 ± 1.6	-
$CoCe/Al_2O_3$	14.2 ± 0.4	12.7 ± 2.2	-	-	26.9 ± 2.6	2.7:1.0
$CoCeMg/Al_2O_3$	10.0 ± 0.5	7.2 ± 1.2	-	3.4 ± 0.1	20.7 ± 0.8	2.8:1.0:2.7
$CoLa/Al_2O_3$	10.3 ± 1.1	-	9.9 ± 0.6	-	20.3 ± 1.6	2.5:1.0
$CoCeLa/Al_2O_3$	7.2 ± 0.6	8.35 ± 0.05	7.9 ± 0.1	-	23.5 ± 0.8	2.0:1.0:1.0

The goal was to produce catalysts with high coverage of the outer surface of the bead by the active metal. Our analysis shows that for every sample, the total metal content shows a sharp increase at the edge of the bead, as is also illustrated in the SEM images in Figure 3. When reduced, this metallic layer at the outer region of the beads can strongly affect the conductivity of the packing material. This, in turn, drastically changes the plasma properties, as is shown in the Lissajous figures and the voltage-current graphs (see below). To monitor the oxidation state of the catalyst metals during plasma operation, *in-situ* experiments would be required, as they could elucidate small differences between different metal combinations.

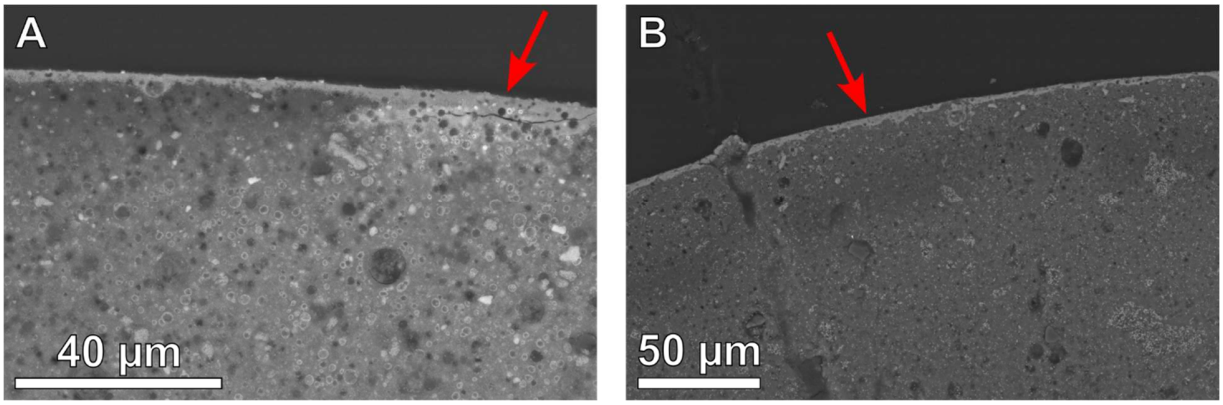

Figure 3. SEM image of CoCe (A) and CoLa (B). The brighter areas at the edge indicate the presence of a higher amount of catalyst elements at the surface of the beads.

3.1.3 N_2 physisorption

The Brunauer-Emmett-Teller (BET) surface area and the pore volume values are listed in Table 2. Coating the Al_2O_3 beads with metals leads to a decrease in surface area and pore volume, due to the coverage of the surface or pore-blocking of the Al_2O_3 support by the metals, as expected. The strongest decrease in surface area compared to pristine Al_2O_3 (207 m^2/g) is in the case of $CoCeMg/Al_2O_3$ (118 m^2/g). Although in our DBD reactor used for plasma-catalytic NH_3 synthesis, the temperature of the gas does not exceed 120 °C [21], the microscale temperature of a site on the catalyst bead may reach much higher temperatures due to the interaction with the microdischarges, which may change the catalyst properties and thus be detrimental for its performance. However, the surface area and pore volume of Co/Al_2O_3, $CoCe/Al_2O_3$, $CoLa/Al_2O_3$ and $CoCeLa/Al_2O_3$ before and after exposure to plasma remain virtually unchanged, indicating the stability of these

catalysts in the plasma discharge. The physisorption isotherms of the fresh and spent catalysts are shown in SI in section S4.

Table 2: The surface area and pore volume of fresh and/or spent Co/Al_2O_3, CoCe/Al_2O_3, CoLa/Al_2O_3, CoCeLa/Al_2O_3 and CoCeMg/Al_2O_3.

Catalyst	**Surface area (m^2/g)**		**Pore volume (cm^3/g)**	
	Fresh	Spent	Fresh	Spent
Al_2O_3	207	-	0.54	-
Co	144	141	0.39	0.36
CoCe	131	132	0.31	0.31
CoLa	152	150	0.37	0.36
CoCeMg	-	118	-	0.30
CoCeLa	143	147	0.33	0.33

3.2 Plasma-catalytic performance

The molar ratio and gas flow rate were varied to find the most optimal conditions for the production of NH_3. Our previous study showed that the 1:1 H_2:N_2 ratio was the ideal feed gas ratio.[21] However, different studies have reported different optimal H_2:N_2 feed gas ratios ranging from 3:1 to 1:2, which suggests that this parameter strongly depends on the plasma characteristics.[21-23, 26] In our study we varied the feed gas ratio to be 3:1, 1:1, and 1:3. As seen in Figure 4, the stoichiometric 3:1 H_2:N_2 ratio yields the highest NH_3 concentration and the lowest EC in two scenarios: the empty reactor and Al_2O_3-packed reactor. Contrary, for the Co-based catalysts, the optimal feed gas ratio shifts towards the 1:1 H_2:N_2 ratio. These findings are in good agreement with reports by Zhu et al. and Gorky et al..[12, 24, 25]

As the packing of the reactor results in a reduction of the effective gas volume inside the reactor, the residence time of the gas inside the packed bed compartment of the reactor would be different compared to an empty reactor, at the same mass flow rate.[21] Based on the work by Uytdenhouwen et al.[45] and given the similar dimensions of our reactor and packing material, we can assume a similar packing efficiency of approximately 50%. Therefore, in terms of residence time, the empty reactor experiments at a gas flow rate of 200 mL/min are comparable to packed reactor

experiments at 100 mL/min. At the same time, in terms of mass flow rate, the empty reactor experiments at a gas flow rate of 100 mL/min are comparable to the packed reactor experiments at 100 mL/min.

It must be noted that a drop in residence time, by increasing the flow rate, could potentially lead both to a drop in the amount of produced NH_3 (due to reduced residence time within the plasma region/packed bed), but also to a higher net NH_3 production (due to reduced possible destruction of the formed NH_3 in the plasma).[46]

Our experiments showed that a higher flow rate of the feed gas mixture yielded a minor decrease in both the concentration and EC of NH_3 production, while the PR increased slightly (Figure S11 in SI). At constant power, the specific energy input (SEI) and gas flow rate are directly reversely proportional and therefore the drop in NH_3 concentration and EC can be linked to the drop SEI at higher flow rates (see formula F4). At constant plasma power, a higher SEI, due to a drop in flowrate, may lead to a larger number of microdischarges and hence higher density of reactive species, which in turn gives more effective collisions. On the other hand, the fraction of high-energy electrons that does not cause any effective collisions also increases resulting in an increase in EC, due to a decrease in flow rate or an increase in SEI.[3, 22, 47] Lastly the PR is proportional to the gas flow rate (Formula F3), thus decreases with decreasing gas flow rate. The effect of the gas flow rate is shown in Figure S11 in SI.

However, it was shown that for an efficient process of plasma-driven NH_3 production with an industrial potential, higher concentrations (at least around 1 vol%, or 10000 ppm) of NH_3 in the reactor exhaust are required.[48, 49] Therefore, despite the higher PR values at higher flow rates, we focus here on the results obtained with a feed gas flow rate of 100 mL/min, which provided the highest NH_3 concentration (Figure 4). The same results, but at a flow rate of 200 mL/min, are presented in Figure S12 in SI.

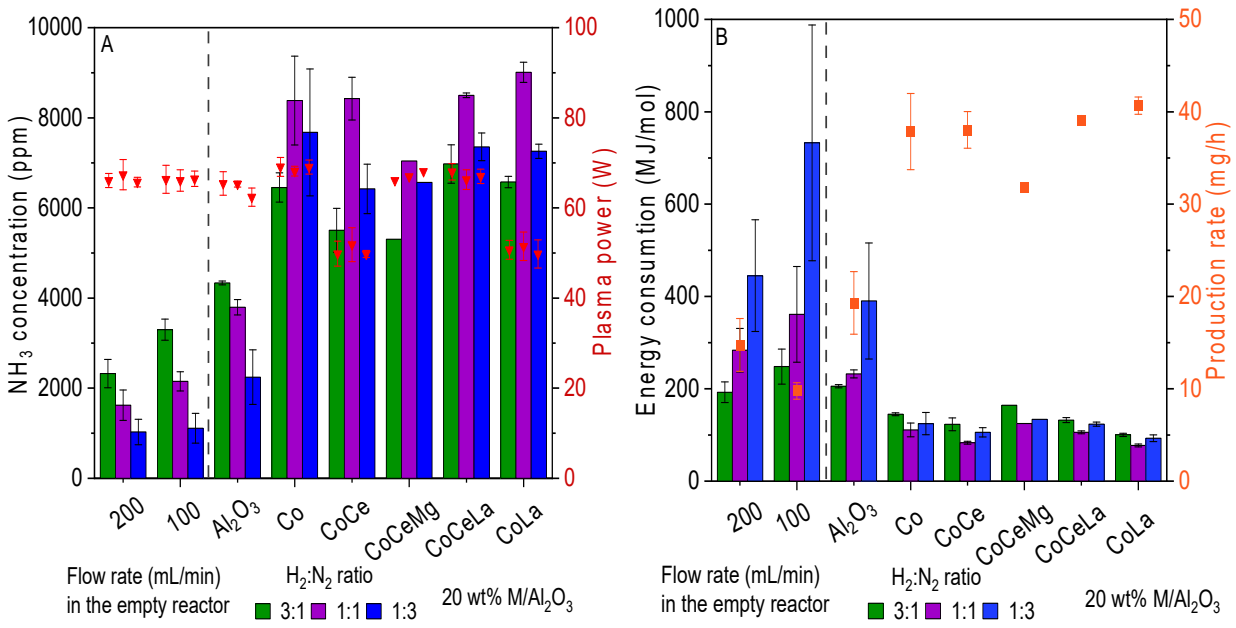

Figure 4. (A) The NH_3 concentration and plasma power, and (B) EC and PR, for an empty DBD reactor, and a DBD reactor packed with Al_2O_3, Co/Al_2O_3, $CoCe/Al_2O_3$, $CoCeMg/Al_2O_3$, $CoCeLa/Al_2O_3$, and $CoLa/Al_2O_3$ catalysts, operating at 100 mL/min and at three different H_2:N_2 ratios. The empty reactor was used with two different feed gas flow rates: 200 and 100 mL/min, to obtain the same residence time and same mass flow rate, respectively, as the packed reactor.

Evidently, even without any packing, some NH_3 is formed due to the plasma performance alone. For the empty DBD reactor with the same apparent residence time, a maximum NH_3 concentration of 2300 ppm and a minimum EC of 192 MJ/mol are obtained, while for the empty DBD reactor with the same gas flow rate, a maximum NH_3 concentration and a minimum EC of 3300 ppm and 248 MJ/mol are obtained at the 3:1 H_2:N_2 ratio, respectively. The PR under these conditions did not exceed 15 mg/h. In an empty reactor, gas phase reactions are dominant. Electron-impact reactions with H_2 and N_2 molecules in the gas phase yield reactive species, ultimately producing NH_3 in the gas phase.

When the packed catalysts are added to the DBD reactor, gas phase reactions occur alongside surface reactions, via Langmuir-Hinschelwood and/or Eley-Rideal reactions, as shown previously.[28] Furthermore, adding a dielectric packing material to the DBD reactor results in an enhancement of the local electric field.[50] This causes higher electron energies, resulting in more

effective inelastic collisions, a higher NH_3 concentration and a lower EC. Indeed, adding pure γ-Al_2O_3 as a packing material to the empty reactor, already results in an increase in NH_3 concentration (4300 ppm) and PR (19 mg/h) and a drop in EC (205 MJ/mol) at the 3:1 H_2:N_2 ratio.

Impregnating the Al_2O_3 support with metals even further improves the NH_3 concentration (8400 ppm), PR (38 mg/h) and EC (111 MJ/mol) for the Co/Al_2O_3 catalyst. This confirms that the addition of metal active sites to alumina has a beneficial effect for plasma catalysis, where in the first approximation the metal sites can facilitate the dissociation of N_2 molecules.[3]

Including additional metals to Co, like Ce, La, CeLa and CeMg, leads to slight variations in PR, NH_3 concentration and EC. Overall, the best results are obtained using CoLa/Al_2O_3 with a maximal NH_3 concentration of 9000 ppm, a PR of 41 mg/h and an EC of 77 MJ/mol at a 1:1 H_2:N_2 ratio and 100 mL/min – despite the fact that the plasma power in the case of CoLa, as well as CoCe, was lower, as seen in Figure 4 (this phenomenon is discussed in the following section). La was reported to improve the dispersion of Co and to function as a structural promoter.[51] Additionally, introduction of La in Co-based catalysts significantly reduces sintering of the catalyst particles due to thermal effects like during calcination.[52] This is confirmed by our XRPD data that did not show any segregated phases of lanthanum (oxides). Hence, small, uniformly distributed La oxide nanoparticles could be formed after calcination, which are below the detection limit of XRPD. The latter is beneficial for the dispersion of other metals. Moreover, the N_2 physisorption analysis showed that adding lanthanum as a co-catalyst slightly increases the specific surface area compared to Co/Al_2O_3 (144 m^2/g), i.e. the highest specific surface area was observed for CoLa/Al_2O_3 (152 m^2/g), in agreement with Zybert et al..[53] For the other bi- and tri-metallic catalysts, the NH_3 concentration, EC and PR values range between 83-125 MJ/mol, 7000-8700 ppm, and 32-39 mg/h, respectively.

Each catalyst was subjected to a total of 18 cycles of plasma experiments of which every cycle lasted ca. 2-3 hours. Figure S13 shows the concentration as a function of time for the reaction using CoLa/Al_2O_3 as packed catalysts. As was shown by the N_2 physisorption analysis, the catalysts remained virtually unchanged after 18 cycles indicating the stability of the catalysts. On the other hand, CoCeMg/Al_2O_3 was only exposed to 6 cycles of plasma experiments before the beads broke, lost integrity and showed discoloration. This could be due to the formation of $MgAl_2O_4$ from MgO and Al_2O_3 which is characterized by a volume expansion of approximately 5%.[54] As a result, the formation of $MgAl_2O_4$ that occurs on the outer surface as well as inside the

pores, causes the beads to break.[55] The XRD patterns show that $MgAl_2O_4$ is already present after calcination and indeed after calcination, a small fraction of beads was already broken. It must be noted that only beads that remained intact were used for the plasma experiments.

In short, the reactor with packed catalysts performs significantly better than the empty reactor and the Al_2O_3-packed reactor, albeit the differences in performance between the different catalysts are not dramatic. Similarly, to the work by Zhang et al. where they used the bimetallic $RuCo/MgTiO_3$ catalyst for non-thermal plasma-assisted NH_3 synthesis, but only observed a minor improvement in ammonia synthesis rate compared to monometallic $Ru/MgTiO_3$ and $Co/MgTiO_3$.[56] At the same time, Rarog-Pilecka et al. reported an increase in thermocatalytic performance of CoCe catalyst with an added metal by ca. 10 times compared to the bimetallic CoCe catalyst.[30] In our work, we used La, however, we did not observe any comparable improvement in the catalyst performance, which underlines that the effects of thermal catalysis cannot be directly adapted into plasma catalysis. In addition, our results confirm earlier model predictions by our group about the importance of radicals (rather than vibrationally excited molecules) and Eley-Rideal reactions in plasma-catalytic NH_3 production.[28]

3.3 Effect of metal composition on plasma discharge

By monitoring the discharge properties (voltage, current and Lissajous figures), we found that the power varied depending on the packed catalyst. In all experiments, we maintained the output power provided by the power supply unit (PSU) constant at 100 W. However, the power deposited into plasma (plasma power) was different for some catalysts. For most systems, the plasma power is ca. 65 W, regardless of the flow rate (see Figure 4A and Figure S12A in SI). Nonetheless, when $CoCe/Al_2O_3$ and $CoLa/Al_2O_3$ are introduced, the plasma power drops to ca. 45-50 W. A higher plasma power could result in a higher NH_3 yield; however, this cannot be tuned at the set PSU power. Yet, for small-scale NH_3 production, an NH_3 yield of 1% might be sufficient[48, 49], and higher yields (potentially obtained at higher power) would come at the cost of a higher EC. In fact, the energy required to separate ca. 1 vol% NH_3 from a gas mixture is in the range of the EC of the HB process (ca. 0.5 MJ/mol).[48, 57] Further research should focus on lowering the EC, and the right choice of catalyst can contribute to that.

To illustrate the changes in the discharge characteristics, Figure 5 presents the Lissajous figures, and Figure 6 shows the current and voltage profiles of only plasma and the plasma using blank Al_2O_3 and Al_2O_3-supported catalysts.

The plasma power is defined as the area enclosed by the Lissajous figures.[23] As seen in Figure 5, the shape of the Lissajous figure varies, depending on the metal composition of the catalyst. Generally, every presented Lissajous figure is almond-shaped, which is typical for discharges with non-uniform gap widths, such as our packed DBD reactor. This type of system will cause the plasma to ignite over a broad range of gap voltages and as a result, the plasma gradually expands during the discharge across the available dielectric area.[31] The differences lie in the slopes of the discharge phase of the Lissajous figures, which vary most significantly as a function of the packed catalyst. The slopes of the Lissajous figures give an indication of the effective capacitance of the system.[58] Specifically, the slopes exhibit the highest increase in the case of CoCe/Al_2O_3, and CoLa/Al_2O_3 compared to pure Al_2O_3 (Figure 5). Indeed, the effective capacitance and the capacitance of the cell when CoCe/Al_2O_3 and CoLa/Al_2O_3 are introduced, are higher than for the other systems, as shown in Table 3. A higher effective capacitance indicates that a more diffuse plasma is generated throughout the entire reaction volume.[58, 59]

Interestingly, this rise in effective capacitance is not observed for the trimetallic CoCeLa/Al_2O_3 catalyst. From the SEM image and the radial distribution of metal content over a CoCeLa/Al_2O_3 bead, shown in Figure S3D and Figure S4D, it is clear that the metal content at the edge of the bead is lower for CoCeLa/Al_2O_3 than for CoLa/Al_2O_3 and CoCe/Al_2O_3. Even though, all catalysts were synthesized via the same method; wet impregnation. As a result, the plasma discharge will not be influenced to the same extent as for the two bimetallic catalysts, hence, a lower effective capacitance is observed for CoCeLa/Al_2O_3.

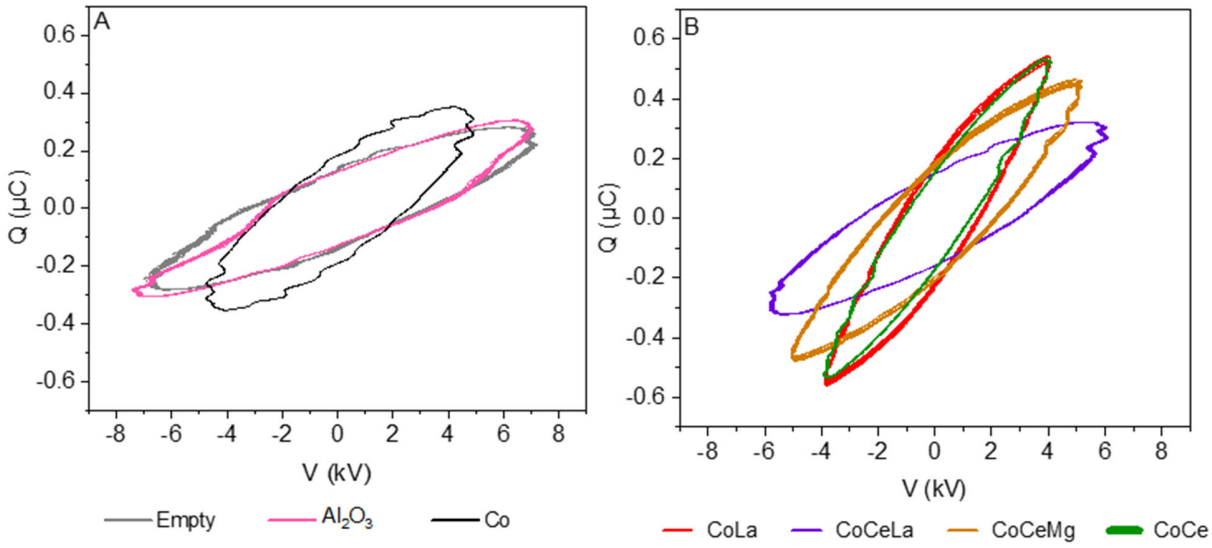

Figure 5. Lissajous plots of the plasma using (A) the empty reactor, pristine Al_2O_3 and Co/Al_2O_3 and (B), $CoLa/Al_2O_3$, $CoCeLa/Al_2O_3$, $CoCeMg/Al_2O_3$ and $CoCe/Al_2O_3$.

Table 3*:The capacitance of the cell and the effective capacitance of a plasma experiment using an empty DBD reactor, and a DBD reactor packed with Al_2O_3, Co/Al_2O_3, $CoCe/Al_2O_3$, $CoCeMg/Al_2O_3$, $CoCeLa/Al_2O_3$, and $CoLa/Al_2O_3$ catalysts, as deduced from the Lissajous plots in Figure 5.*

Catalyst	**C_{Cell} (pF)**	**C_{Eff} (pF)**
Empty reactor	14 ± 2	83 ± 3
Al_2O_3	19.08 ± 0.03	105 ± 22
Co/Al_2O_3	45.7 ± 0.3	168 ± 3
$CoCe/Al_2O_3$	67 ± 1	211 ± 4
$CoCeMg/Al_2O_3$	47 ± 10	163 ± 7
$CoCeLa/Al_2O_3$	26 ± 3	145 ± 31
$CoLa/Al_2O_3$	72 ± 9	218 ± 21

The aforementioned shift in plasma behaviour can also be observed from the current waveform profiles, as plotted in Figure 6. The peaks in the current profile (sharp "spikes" at the extrema of the current sine) correspond to the microdischarges. The empty reactor displays typical filamentary discharges, shown in Figure S9. When introducing Al_2O_3 into the reactor, the number and the intensity of these spikes increases compared to the empty reactor. A larger number of microdischarges results in the generation of more high energy electrons and reactive nitrogen and hydrogen species, hence a higher NH_3 formation. On the other hand, the higher electron density can also result in more NH_3 decomposition by electron impact reactions.[46, 60, 61]

When Co-based catalysts are introduced, both the intensity and the number of the microdischarges decrease compared to Al_2O_3 packing and the empty reactor (Figure 6), although the NH_3 concentration and PR are higher (and hence the EC is lower) (Figure 4 and Figure S12 in SI). Therefore, we imply that these improvements in NH_3 concentration, EC and PR are the result of (i) a change in reaction mechanism, due to the presence of the metal sites on the Co-based catalysts as well as (ii) a change in plasma discharge properties.

Furthermore, depending on the exact metal composition of the catalyst, the current profile also varies strongly. The most significant difference is once more observed for $CoCe/Al_2O_3$, and $CoLa/Al_2O_3$. Unlike the current profiles in the presence of the other catalysts, Al_2O_3 and plasma only, there are clearly fewer microdischarges, indicating a more difuse plasma instead of a filamentary discharge, when these two catalysts are introduced. [40] A similar change in the discharge profiles was observed by Patil et al. however they only discussed the decreased number of microdischarges and not the change of the overall discharge mode.[4] A decrease in the amount of microdischarges results in less NH_3 decomposition and explains why even at lower plasma power, $CoCe/Al_2O_3$, and $CoLa/Al_2O_3$ show the highest performance.[60]

Additionally, once the Al_2O_3 beads are impregnated with a metal oxide which is further reduced to the respective metal, the conductivity of the beads increases. We believe that $CoCe/Al_2O_3$ and $CoLa/Al_2O_3$ show higher electrical conductivity after reduction, compared to the other catalysts. Conductive materials can promote charge transfer in the plasma discharge by improving the charge carrier mobility.[62] As a result, the charge is more spread over the surface of the beads, causing a change in the discharge properties.[63] A similar change in plasma behaviour was also observed by Pribyl et al. after introducing 20 wt% $MgAl_2O_4$ supported on Al_2O_3, in their DBD reactor.[64]

On the contrary, in a study conducted by Herrera et al. various 5 wt% transition metal catalysts supported on Al_2O_3 were synthesized however, they did not observe any statistical difference in plasma properties, specifically in terms of capacitance and filamentary current behaviour.[65] Yet, the difference with our study lies in the total metal loading of the catalysts, which is 20 wt% in our case. As mentioned earlier, this metal loading was chosen to increase the fraction of metals on the support surface. Indeed, our SEM-EDX analysis showed that there is a sharp increase in metal content at the edge of the bead which affected the plasma behaviour. Moreover, in the study by Herrera et al. only 17% of the discharge interacted with the catalysts meaning that it is possible that any effects the catalyst may have on the plasma, only occur in such a small fraction of the overall plasma volume, that they are not reflected in their measurements. While in our study, the entire plasma volume was packed with catalysts so their effect on the plasma behaviour will influence our measurements.

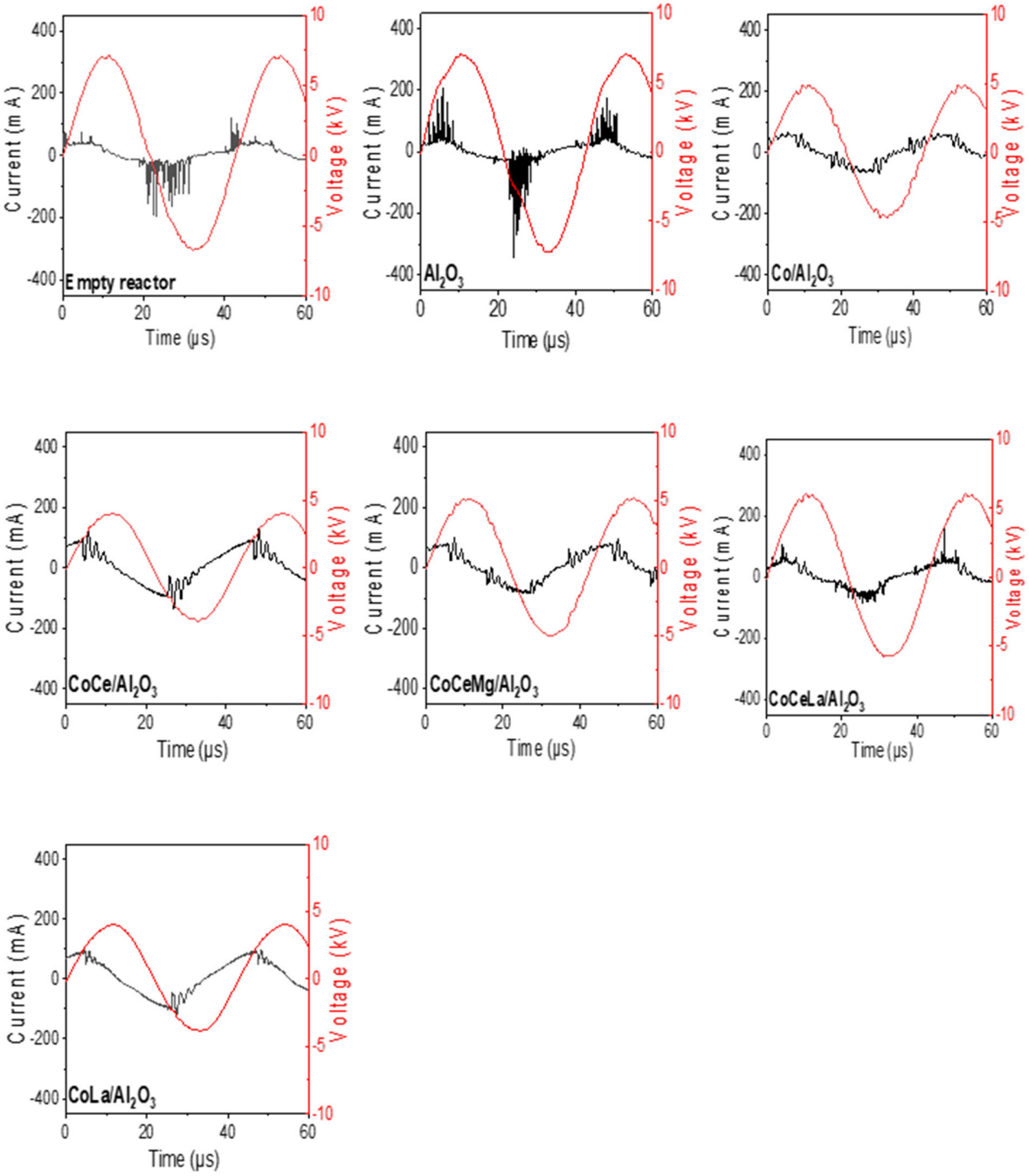

Figure 6. Current and voltage profiles observed in the empty DBD reactor and the DBD reactor packed with pristine Al_2O_3 and the different Al_2O_3-supported catalysts.

In summary, these data suggest that the catalysts act as plasma modifiers, i.e., they change the discharge properties and thus the gas phase plasma chemistry. At the same time, we showed that

when the discharge properties are similar, the metal composition of the catalyst does not have a strong effect on the reaction performance, as seen in Figure 4 and Figure S12 in SI, as well as in our previous work.[21] Taken together, our results indicate that our catalysts used in plasma-catalytic NH_3 synthesis act more as plasma modifiers, and that this effect dominates over the direct catalytic effect governed by the chemistry on the catalyst surface.

5. Conclusion

We studied plasma-catalytic NH_3 synthesis over various catalysts (20 wt% Co/Al_2O_3, $CoCe/Al_2O_3$, $CoLa/Al_2O_3$, $CoCeLa/Al_2O_3$ and $CoCeMg/Al_2O_3$) in a DBD plasma reactor. The catalysts were synthesized via wet impregnation, and the structural and physicochemical properties of the catalysts were determined via XRPD, Raman spectroscopy, SEM-EDX and N_2 physisorption.

Introducing the transition metal catalysts into the reactor yielded an enhancement of more than 4 times in NH_3 concentration and in PR and a reduction of ca. 5 times in EC, as obtained with the $CoLa/Al_2O_3$ catalyst, compared to the empty reactor at the same 1:1 H_2:N_2 ratio and the same flow rate of 100 mL/min. Yet, the difference in plasma-catalytic performance between the various Co-based catalysts was limited, in line with previous model predictions and experimental observations by our group and others [3, 18, 21, 28, 29]

Instead, we observed significant differences in plasma properties as a function of the metal composition of the catalyst. Depending on the catalyst, the plasma characteristics, such as the deposited power and the current profile, change drastically, unambiguously indicating that the catalysts act as plasma modifiers. While the chemical composition of the catalysts under the same plasma properties did not change the reaction performance significantly, the changes in plasma properties resulted in a considerable improvement by reducing the EC. Hence, the "plasma modifier" effect of the catalysts dominates over the direct catalytic effect defined by the chemistry on the catalyst surface. Our findings suggest that the performance of the plasma-catalytic NH_3 synthesis can be tuned by employing catalysts which change the plasma properties to the desired mode, e.g. fewer microdischarges and a shift towards the diffuse discharge mode, as demonstrated in our work. Moreover, the right choice of catalyst could result in a lower deposited power and as a result, a lower energy consumption. Assigning the specific effects is the subject of future investigations.

We are aware that the metals used in this study namely Co, Mg, La and Ce, are Critical Raw Materials and are thus subject to a supply risk.[66] However, our findings showed that the composition of the catalyst does not have a dramatic effect in terms of "classical" catalytic effects.[21] As a result, different metals could be used as catalysts for the plasma-catalytic synthesis of NH_3 – as long as the plasma discharge properties remain optimal for the reaction.

Our study reveals an important phenomenon for further developments of plasma technology, and emphasizes the inapplicability of direct translation of chemical knowledge from thermal catalysis into plasma-catalytic systems.

Associated content

Supporting information: experimental details on synthesis and plasma setup, additional characterization details and experimental data.

Author information

Corresponding author

Callie Ndayirinde - Research group PLASMANT, Department of Chemistry, University of Antwerp, Universiteitsplein 1, B-2610 Wilrijk-Antwerp, Belgium. Email: callie.ndayirinde@uantwerpen.be

Authors

Yury Gorbanev - Research group PLASMANT, Department of Chemistry, University of Antwerp, Universiteitsplein 1, B-2610 Wilrijk-Antwerp, Belgium.

Radu-George Ciocarlan - Research group LADCA, Department of Chemistry, University of Antwerp, Universiteitsplein 1, B-2610 Wilrijk-Antwerp, Belgium.

Alessandro Smets - Research group PLASMANT, Department of Chemistry, University of Antwerp, Universiteitsplein 1, B-2610 Wilrijk-Antwerp, Belgium; Research group LADCA, Department of Chemistry, University of Antwerp, Universiteitsplein 1, B-2610 Wilrijk-Antwerp, Belgium.

Evgenii Vlasov - Research group EMAT, Department of Physics, University of Antwerp, Groenenborgerlaan 171, 2020 Antwerp, Belgium

Robin De Meyer - Research group PLASMANT, Department of Chemistry, University of Antwerp, Universiteitsplein 1, B-2610 Wilrijk-Antwerp, Belgium; Research group EMAT, Department of Physics, University of Antwerp, Groenenborgerlaan 171, 2020 Antwerp, Belgium

Sara Bals - Research group EMAT, Department of Physics, University of Antwerp, Groenenborgerlaan 171, 2020 Antwerp, Belgium

Pegie Cool - Research group LADCA, Department of Chemistry, University of Antwerp, Universiteitsplein 1, B-2610 Wilrijk-Antwerp, Belgium.

Annemie Bogaerts - Research group PLASMANT, Department of Chemistry, University of Antwerp, Universiteitsplein 1, B-2610 Wilrijk-Antwerp, Belgium.

Author Contributions

Callie Ndayirinde: Conceptualization, Methodology, Investigation, Writing-Original Draft, Visualization **Yury Gorbanev:** Conceptualization, Methodology, Writing - Review & Editing, Supervision **Radu-George Ciocarlan:** Conceptualization, Methodology, Writing - Review & Editing, Supervision **Alessandro Smets:** Investigation **Evgenii Vlasov:** Investigation

The manuscript was written through contributions of all authors. All authors have given approval to the final version of the manuscript.

Acknowledgement

This research was supported by the European Research Council (ERC) under the European Union's Horizon 2020 research and innovation programme (grant agreement No 810182 – SCOPE ERC Synergy project) and the Methusalem project of the University of Antwerp.

Abbreviations

HB, Haber-Bosch; NTP, non-thermal plasma; DBD, dielectric barrier discharge, XRPD; X-ray powder diffraction; SEM, scanning electron microscopy; EDX, energy dispersive X-ray spectroscopy; BET, Brunauer-Emmett-Teller; EC, energy consumption; PR, production rate; SEI, specific energy input

6. REFERENCES

(1) United Nations. *World population prospects: The 2019 Revison*; United Nations-, 2019.
(2) FAO, F. The future of food and agriculture–Trends and challenges. *Annual Report* **2017**.
(3) Wang, Y.; Craven, M.; Yu, X.; Ding, J.; Bryant, P.; Huang, J.; Tu, X. Plasma-Enhanced Catalytic Synthesis of Ammonia over a Ni/Al2O3 Catalyst at Near-Room Temperature: Insights into the Importance of the Catalyst Surface on the Reaction Mechanism. *ACS Catal.* **2019**, *9* (12), 10780-10793. DOI: 10.1021/acscatal.9b02538.
(4) Patil, B. S.; Cherkasov, N.; Srinath, N. V.; Lang, J.; Ibhadon, A. O.; Wang, Q.; Hessel, V. The role of heterogeneous catalysts in the plasma-catalytic ammonia synthesis. *Catal. Today* **2021**, *362*, 2-10. DOI: 10.1016/j.cattod.2020.06.074.
(5) Rouwenhorst, K. H.; Burbach, H. G.; Vogel, D. W.; Paulí, J. N.; Geerdink, B.; Lefferts, L. Plasma-catalytic ammonia synthesis beyond thermal equilibrium on Ru-based catalysts in non-thermal plasma. *Catal. Sci. Technol.* **2021**. DOI: 10.1039/D0CY02189J.
(6) Montoya, J. H.; Tsai, C.; Vojvodic, A.; Nørskov, J. K. The Challenge of Electrochemical Ammonia Synthesis: A New Perspective on the Role of Nitrogen Scaling Relations. *ChemSusChem* **2015**, *8* (13), 2180-2186. DOI: 10.1002/cssc.201500322.
(7) Kyriakou, V.; Garagounis, I.; Vourros, A.; Vasileiou, E.; Stoukides, M. An electrochemical haber-bosch process. *Joule* **2020**, *4* (1), 142-158. DOI: 10.1016/j.joule.2019.10.006.
(8) Wang, Y.; Meyer, T. J. A Route to Renewable Energy Triggered by the Haber-Bosch Process. *Chem* **2019**, *5* (3), 496-497. DOI: 10.1016/j.chempr.2019.02.021.
(9) Lan, R.; Irvine, J. T.; Tao, S. Synthesis of ammonia directly from air and water at ambient temperature and pressure. *Sci. Rep.* **2013**, *3* (1), 1-7. DOI: 10.1038/srep01145.
(10) Ghavam, S.; Vahdati, M.; Wilson, I.; Styring, P. Sustainable ammonia production processes. *Front. Energy Res.* **2021**, *9*, 34. DOI: 10.3389/fenrg.2021.580808.
(11) Schiffer, Z. J.; Manthiram, K. Electrification and decarbonization of the chemical industry. *Joule* **2017**, *1* (1), 10-14. DOI: 10.1016/j.joule.2017.07.008.
(12) Gorky, F.; Best, A.; Jasinski, J.; Allen, B. J.; Alba-Rubio, A. C.; Carreon, M. L. Plasma catalytic ammonia synthesis on Ni nanoparticles: The size effect. *J. Catal.* **2021**, *393*, 369-380. DOI: 10.1016/j.jcat.2020.11.030.
(13) Bogaerts, A.; Tu, X.; Whitehead, J. C.; Centi, G.; Lefferts, L.; Guaitella, O.; Azzolina-Jury, F.; Kim, H.-H.; Murphy, A. B.; Schneider, W. F.; et al. The 2020 plasma catalysis roadmap. *J. Phys. D: Appl. Phys.* **2020**, *53* (44). DOI: 10.1088/1361-6463/ab9048.
(14) Rouwenhorst, K. H. R.; Engelmann, Y.; van 't Veer, K.; Postma, R. S.; Bogaerts, A.; Lefferts, L. Plasma-driven catalysis: green ammonia synthesis with intermittent electricity. *Green Chem.* **2020**, *22* (19), 6258-6287. DOI: 10.1039/d0gc02058c.
(15) Patil, B. S.; Wang, Q.; Hessel, V.; Lang, J. Plasma N2-fixation: 1900–2014. *Catal. Today* **2015**, *256*, 49-66. DOI: 10.1016/j.cattod.2015.05.005.
(16) Bogaerts, A.; Neyts, E. C.; Guaitella, O.; Murphy, A. B. Foundations of plasma catalysis for environmental applications. *Plasma Sources Sci. Technol.* **2022**, *31* (5). DOI: 10.1088/1361-6595/ac5f8e.
(17) Wang, Y.; Yang, W.; Xu, S.; Zhao, S.; Chen, G.; Weidenkaff, A.; Hardacre, C.; Fan, X.; Huang, J.; Tu, X. Shielding protection by mesoporous catalysts for improving plasma-catalytic ambient ammonia synthesis. *Journal of the American Chemical Society* **2022**. DOI: 10.1021/jacs.2c01950.
(18) Mehta, P.; Barboun, P.; Herrera, F. A.; Kim, J.; Rumbach, P.; Go, D. B.; Hicks, J. C.; Schneider, W. F. Overcoming ammonia synthesis scaling relations with plasma-enabled catalysis. *Nat. Catal.* **2018**, *1* (4), 269-275. DOI: 10.1038/s41929-018-0045-1.

(19) Liu, Y.; Wang, C.-W.; Xu, X.-F.; Liu, B.-W.; Zhang, G.-M.; Liu, Z.-W.; Chen, Q.; Zhang, H.-B. Synergistic Effect of Co–Ni Bimetal on Plasma Catalytic Ammonia Synthesis. *Plasma Chem. Plasma Process.* **2022**, 1-16. DOI: 10.1007/s11090-021-10223-1.
(20) Barboun, P.; Mehta, P.; Herrera, F. A.; Go, D. B.; Schneider, W. F.; Hicks, J. C. Distinguishing Plasma Contributions to Catalyst Performance in Plasma-Assisted Ammonia Synthesis. *ACS Sustain. Chem. Eng.* **2019**, *7* (9), 8621-8630. DOI: 10.1021/acssuschemeng.9b00406.
(21) Gorbanev, Y.; Engelmann, Y.; van't Veer, K.; Vlasov, E.; Ndayirinde, C.; Yi, Y.; Bals, S.; Bogaerts, A. Al2O3-Supported Transition Metals for Plasma-Catalytic NH3 Synthesis in a DBD Plasma: Metal Activity and Insights into Mechanisms. *Catalysts* **2021**, *11* (10). DOI: 10.3390/catal11101230.
(22) Li, S.; van Raak, T.; Gallucci, F. Investigating the operation parameters for ammonia synthesis in dielectric barrier discharge reactors. *J. Phys. D: Appl. Phys.* **2020**, *53* (1). DOI: 10.1088/1361-6463/ab4b37.
(23) Xie, Q.; Zhuge, S.; Song, X.; Lu, M.; Yu, F.; Ruan, R.; Nie, Y. Non-thermal atmospheric plasma synthesis of ammonia in a DBD reactor packed with various catalysts. *J. Phys. D: Appl. Phys.* **2019**, *53* (6), 064002. DOI: 10.1088/1361-6463/ab57e5.
(24) Zhu, X.; Hu, X.; Wu, X.; Cai, Y.; Zhang, H.; Tu, X. Ammonia synthesis over γ-Al2O3 pellets in a packed-bed dielectric barrier discharge reactor. *J. Phys. D: Appl. Phys.* **2020**, *53* (16), 164002. DOI: 10.1088/1361-6463/ab6cd1.
(25) Zhu, X.; Liu, J.; Hu, X.; Zhou, Z.; Li, X.; Wang, W.; Wu, R.; Tu, X. Plasma-catalytic synthesis of ammonia over Ru-based catalysts: Insights into the support effect. *J. Energy Inst.* **2022**, *102*, 240-246. DOI: 10.1016/j.joei.2022.02.014.
(26) Hu, X.; Zhu, X.; Wu, X.; Cai, Y.; Tu, X. Plasma-enhanced NH3 synthesis over activated carbon-based catalysts: Effect of active metal phase. *Plasma Process Polym* **2020**, *17* (12), 2000072. DOI: 10.1002/ppap.202000072.
(27) Akay, G.; Zhang, K. Process intensification in ammonia synthesis using novel coassembled supported microporous catalysts promoted by nonthermal plasma. *Ind. Eng. Chem. Res.* **2017**, *56* (2), 457-468. DOI: 10.1021/acs.iecr.6b02053.
(28) Engelmann, Y.; van 't Veer, K.; Gorbanev, Y.; Neyts, E. C.; Schneider, W. F.; Bogaerts, A. Plasma Catalysis for Ammonia Synthesis: A Microkinetic Modeling Study on the Contributions of Eley–Rideal Reactions. *ACS Sustain. Chem. Eng.* **2021**, *9* (39), 13151-13163. DOI: 10.1021/acssuschemeng.1c02713.
(29) Shah, J.; Gorky, F.; Psarras, P.; Seong, B.; Gómez-Gualdrón, D. A.; Carreon, M. L. Enhancement of the Yield of Ammonia by Hydrogen-Sink Effect during Plasma Catalysis. *ChemCatChem* **2019**, *12* (4), 1200-1211. DOI: 10.1002/cctc.201901769.
(30) Raróg-Pilecka, W.; Karolewska, M.; Truszkiewicz, E.; Iwanek, E.; Mierzwa, B. Cobalt Catalyst Doped with Cerium and Barium Obtained by Co-Precipitation Method for Ammonia Synthesis Process. *Catal. Lett.* **2011**, *141* (5), 678-684. DOI: 10.1007/s10562-011-0564-8.
(31) Peeters, F.; Butterworth, T. Electrical diagnostics of dielectric barrier discharges. In *Atmospheric Pressure Plasma: from Diagnostics to Applications*, Anton Nikiforov, Z. C. Ed.; BoD – Books on Demand, 2019; p 144.
(32) Vervloessem, E.; Gorbanev, Y.; Nikiforov, A.; De Geyter, N.; Bogaerts, A. Sustainable NOx production from air in pulsed plasma: elucidating the chemistry behind the low energy consumption. *Green Chem.* **2022**, *24* (2), 916-929. DOI: 10.1039/d1gc02762j.
(33) King, C. *Do you know why Mass Flow reference conditions matter?* Bronkhorst, 2019. https://www.bronkhorst.com/int/blog-1/do-you-know-why-mass-flow-reference-conditions-matter/ (accessed 2022 November 11).
(34) Zhang, L.; Zhao, X.; Ma, W.; Wu, M.; Qian, N.; Lu, W. Novel three-dimensional Co 3 O 4 dendritic superstructures: hydrothermal synthesis, formation mechanism and magnetic properties. *CrystEngComm* **2013**, *15* (7), 1389-1396. DOI: 10.1039/C2CE26374B.

(35) Duan, X.; Pan, M.; Yu, F.; Yuan, D. Synthesis, structure and optical properties of CoAl2O4 spinel nanocrystals. *J. Alloys Compd.* **2011**, *509* (3), 1079-1083. DOI: 10.1016/j.jallcom.2010.09.199.
(36) Srisawad, N.; Chaitree, W.; Mekasuwandumrong, O.; Praserthdam, P.; Panpranot, J. Formation of CoAl2O4Nanoparticles via Low-Temperature Solid-State Reaction of Fine Gibbsite and Cobalt Precursor. *Journal of Nanomaterials* **2012**, *2012*, 1-8. DOI: 10.1155/2012/108369.
(37) Kim, K. S.; Park, Y. J. Catalytic properties of Co3O4 nanoparticles for rechargeable Li/air batteries. *Nanoscale Research Letters* **2012**, *7* (1). DOI: 10.1186/1556-276x-7-47.
(38) Kanwal, F.; Batool, A.; Adnan, M.; Naseem, S. The effect of molecular structure, band gap energy and morphology on the dc electrical conductivity of polyaniline/aluminium oxide composites. *Mater. Res. Innovations* **2015**, *19* (sup8), S8-354-S358-358. DOI: 10.1179/1432891715Z.0000000001688.
(39) Gurram, V. R. B.; Enumula, S. S.; Mutyala, S.; Pochamoni, R.; Prasad, P. S. S.; Burri, D. R.; Kamaraju, S. R. R. The advantage of ceria loading over V2O5/Al2O3 catalyst for vapor phase oxidative dehydrogenation of ethylbenzene to styrene using CO2 as a soft oxidant. *Applied Petrochemical Research* **2016**, *6* (4), 427-437. DOI: 10.1007/s13203-016-0163-0.
(40) Xue, S.-F.; Wu, W.-Y.; Bian, X.; Wang, Z.-F.; Wu, Y.-F. Facile preparation of CeO2 microspheres with high surface area by ultrasonic spray pyrolysis. *Green Processing and Synthesis* **2018**, *7* (3), 241-247. DOI: 10.1515/gps-2017-0041.
(41) Wang, J.; Li, Z.; Zhang, S.; Yan, S.; Cao, B.; Wang, Z.; Fu, Y. Enhanced NH3 gas-sensing performance of silica modified CeO2 nanostructure based sensors. *Sensors and Actuators B: Chemical* **2018**, *255*, 862-870. DOI: 10.1016/j.snb.2017.08.149.
(42) Deori, K.; Deka, S. Morphology oriented surfactant dependent CoO and reaction time dependent Co 3 O 4 nanocrystals from single synthesis method and their optical and magnetic properties. *CrystEngComm* **2013**, *15* (42), 8465-8474. Sui, Y.; Zhao, Y.; Zhang, J.; Jaswal, S.; Li, X.; Sellmyer, D. Ferromagnetic multipods fabricated by solution phase synthesis and hydrogen reduction. *IEEE Trans. Magn.* **2007**, *43* (6), 3115-3117. Zhao, X.; Ceresoli, D.; Vanderbilt, D. Structural, electronic, and dielectric properties of amorphous Zr O 2 from ab initio molecular dynamics. *Physical Review B* **2005**, *71* (8), 085107.
(43) Zhang, Q.-Z.; Bogaerts, A. Propagation of a plasma streamer in catalyst pores. *Plasma Sources Sci. Technol.* **2018**, *27* (3), 035009. DOI: 10.1088/1361-6595/aab47a.
(44) Hargreaves, J. S. J.; Chung, Y.-M.; Ahn, W.-S.; Hisatomi, T.; Domen, K.; Kung, M. C.; Kung, H. H. Minimizing energy demand and environmental impact for sustainable NH3 and H2O2 production—A perspective on contributions from thermal, electro-, and photo-catalysis. *Appl. Catal.* **2020**, *594*. DOI: 10.1016/j.apcata.2020.117419.
(45) Uytdenhouwen, Y.; Bal, K. M.; Michielsen, I.; Neyts, E. C.; Meynen, V.; Cool, P.; Bogaerts, A. How process parameters and packing materials tune chemical equilibrium and kinetics in plasma-based CO2 conversion. *Chem. Eng. J.* **2019**, *372*, 1253-1264. DOI: 10.1016/j.cej.2019.05.008.
(46) van 't Veer, K.; Engelmann, Y.; Reniers, F.; Bogaerts, A. Plasma-catalytic ammonia synthesis in a DBD plasma: role of microdischarges and their afterglows. *J. Phys. Chem. C* **2020**, *124* (42), 22871-22883. DOI: 10.1021/acs.jpcc.0c05110.
(47) Kim, H. H.; Teramoto, Y.; Ogata, A.; Takagi, H.; Nanba, T. Atmospheric-pressure nonthermal plasma synthesis of ammonia over ruthenium catalysts. *Plasma Process Polym* **2017**, *14* (6), 1600157.
(48) Hollevoet, L.; Jardali, F.; Gorbanev, Y.; Creel, J.; Bogaerts, A.; Martens, J. A. Towards Green Ammonia Synthesis through Plasma-Driven Nitrogen Oxidation and Catalytic Reduction. *Angew. Chem. Int. Ed.* **2020**, *59* (52), 23825-23829. DOI: 10.1002/anie.202011676.
(49) Hollevoet, L.; Vervloessem, E.; Gorbanev, Y.; Nikiforov, A.; De Geyter, N.; Bogaerts, A.; Martens, J. A. Energy-Efficient Small-Scale Ammonia Synthesis Process with Plasma-enabled Nitrogen Oxidation and Catalytic Reduction of Adsorbed NOx. *ChemSusChem* **2022**, e202102526. DOI: 10.1002/cssc.202102526.

(50) Van Laer, K.; Bogaerts, A. Influence of Gap Size and Dielectric Constant of the Packing Material on the Plasma Behaviour in a Packed Bed DBD Reactor: A Fluid Modelling Study. *Plasma Process Polym* **2017**, *14* (4-5). DOI: 10.1002/ppap.201600129.
(51) Zybert, M.; Karasińska, M.; Truszkiewicz, E.; Mierzwa, B.; Raróg-Pilecka, W. Properties and activity of the cobalt catalysts for NH3 synthesis obtained by co-precipitation – the effect of lanthanum addition. *Pol. J. Chem. Technol.* **2015**, *17* (1), 138-143. DOI: 10.1515/pjct-2015-0020.
(52) Xun, Y.; He, X.; Yan, H.; Gao, Z.; Jin, Z.; Jia, C. Fe- and Co-doped lanthanum oxides catalysts for ammonia decomposition: Structure and catalytic performances. *J. Rare Earths* **2017**, *35* (1), 15-23. DOI: 10.1016/s1002-0721(16)60167-9.
(53) Zybert, M.; Tarka, A.; Mierzwa, B.; Kępiński, L.; Raróg-Pilecka, W. Promotion effect of lanthanum on the Co/La/Ba ammonia synthesis catalysts—the influence of lanthanum content. *Appl. Catal.* **2016**, *515*, 16-24. DOI: 10.1016/j.apcata.2016.01.036.
(54) Mazzoni, A. D.; Sainz, M. A.; Caballero, A.; Aglietti, E. F. Formation and sintering of spinels (MgAl2O4) in reducing atmospheres. *Mater. Chem. Phys.* **2003**, *78* (1), 30-37. DOI: 10.1016/s0254-0584(02)00333-4. Rooi Ping, L.; Azad, A.-M.; Wan Dung, T. Magnesium aluminate (MgAl2O4) spinel produced via self-heat-sustained (SHS) technique. *Mater. Res. Bull.* **2001**, *36* (7-8), 1417-1430. DOI: 10.1016/s0025-5408(01)00622-5.
(55) Zhang, P.; Chen, A.; Ding, D.; Gao, S.; Liu, X.; Ye, G.; Liao, G. Trace nanoscale Al2O3 in Al2O3-MgAl2O4 castable for improved thermal shock performance. *Ceram. Int.* **2019**, *45* (17), 23029-23036. DOI: 10.1016/j.ceramint.2019.07.350.
(56) Zhang, Y.; Li, S.; Yuan, Z.; Chen, H.; Fan, X. Mechanochemical Synthesis of RuCo/MgTiO3 Catalysts for Nonthermal Plasma-Assisted Ammonia Synthesis. *Ind. Eng. Chem. Res.* **2022**, *61* (38), 14199-14210. DOI: 10.1021/acs.iecr.2c02216.
(57) Cherkasov, N.; Ibhadon, A.; Fitzpatrick, P. A review of the existing and alternative methods for greener nitrogen fixation. *Chem. Eng. Process.* **2015**, *90*, 24-33. DOI: 10.1016/j.cep.2015.02.004.
(58) Ramakers, M.; Michielsen, I.; Aerts, R.; Meynen, V.; Bogaerts, A. Effect of Argon or Helium on the CO2Conversion in a Dielectric Barrier Discharge. *Plasma Process Polym* **2015**, *12* (8), 755-763. DOI: 10.1002/ppap.201400213.
(59) Uytdenhouwen, Y.; Van Alphen, S.; Michielsen, I.; Meynen, V.; Cool, P.; Bogaerts, A. A packed-bed DBD micro plasma reactor for CO2 dissociation: Does size matter? *Chem. Eng. J.* **2018**, *348*, 557-568. DOI: 10.1016/j.cej.2018.04.210.
(60) Andersen, J. A.; Christensen, J. M.; Østberg, M.; Bogaerts, A.; Jensen, A. D. Plasma-catalytic ammonia decomposition using a packed-bed dielectric barrier discharge reactor. *Int. J. Hydrogen Energy* **2022**, *47* (75), 32081-32091. DOI: 10.1016/j.ijhydene.2022.07.102.
(61) Gorky, F.; Lucero, J. M.; Crawford, J. M.; Blake, B. A.; Guthrie, S. R.; Carreon, M. A.; Carreon, M. L. Insights on cold plasma ammonia synthesis and decomposition using alkaline earth metal-based perovskites. *Catal. Sci. Technol.* **2021**, *11* (15), 5109-5118. DOI: 10.1039/d1cy00729g. Navascués, P.; Obrero-Pérez, J. M.; Cotrino, J.; González-Elipe, A. R.; Gómez-Ramírez, A. Unraveling Discharge and Surface Mechanisms in Plasma-Assisted Ammonia Reactions. *ACS Sustain. Chem. Eng.* **2020**, *8* (39), 14855-14866. DOI: 10.1021/acssuschemeng.0c04461. van't Veer, K.; Van Alphen, S.; Remy, A.; Gorbanev, Y.; De Geyter, N.; Snyders, R.; Reniers, F.; Bogaerts, A. Spatially and temporally non-uniform plasmas: microdischarges from the perspective of molecules in a packed bed plasma reactor. *J. Phys. D: Appl. Phys.* **2021**, *54* (17), 174002. DOI: 10.1088/1361-6463/abe15b.
(62) Tu, X.; Gallon, H. J.; Twigg, M. V.; Gorry, P. A.; Whitehead, J. C. Dry reforming of methane over a Ni/Al2O3 catalyst in a coaxial dielectric barrier discharge reactor. *J. Phys. D: Appl. Phys.* **2011**, *44* (27), 274007. DOI: 10.1088/0022-3727/44/27/274007.

(63) Naude, N.; Massines, F. Influence of the surface conductivity on the stability of a glow dielectric-barrier discharge. *IEEE Trans Plasma Sci* **2008**, *36* (4), 1322-1323. DOI: 10.1109/TPS.2008.923899.
(64) Pribyl, R.; Stastny, P.; Pazderka, M.; Kelar, J.; Kelar Tucekova, Z.; Zemanek, M.; Trunec, M.; Cernak, M. Properties of MgAl2O4 doped alumina barrier layers for dielectric barrier discharge. *J. Phys. D: Appl. Phys.* **2020**, *53* (50). DOI: 10.1088/1361-6463/abb0ba.
(65) Herrera, F. A.; Brown, G. H.; Barboun, P.; Turan, N.; Mehta, P.; Schneider, W. F.; Hicks, J. C.; Go, D. B. The impact of transition metal catalysts on macroscopic dielectric barrier discharge (DBD) characteristics in an ammonia synthesis plasma catalysis reactor. *J. Phys. D: Appl. Phys.* **2019**, *52* (22), 224002.
(66) Hofmann, M.; Hofmann, H.; Hagelüken, C.; Hool, A. Critical raw materials: A perspective from the materials science community. *Sustainable Materials and Technologies* **2018**, *17*. DOI: 10.1016/j.susmat.2018.e00074.

Plasma-catalytic ammonia synthesis: packed catalysts act as plasma modifiers

Callie Ndayirinde[1], Yury Gorbanev[1], Radu-George Ciocarlan[2], Alessandro Smets[1,2], Evgenii Vlasov[3], Robin De Meyer[1,3], Sara Bals[3], Pegie Cool[2], Annemie Bogaerts[1]

[1]Research group PLASMANT, Department of Chemistry, University of Antwerp, Universiteitsplein 1, B-2610 Wilrijk-Antwerp, Belgium.

[2]Research group LADCA, Department of Chemistry, University of Antwerp, Universiteitsplein 1, B-2610 Wilrijk-Antwerp, Belgium.

[3]Research group EMAT, Department of Physics, University of Antwerp, Groenenborgerlaan 171, 2020 Antwerp, Belgium

Supporting information

Pages: 16

Figures: 9

Tables: 4

Table of contents

***Table S1**: A summary of studies on NH_3 production from N_2 and H_2 in dielectric barrier discharge (DBD) plasma reactors, as well as comparison with our work. The catalysts, experimental details, and the calculated values of NH_3 yield and production rate correspond to the lowest energy consumption (EC) reported in the respective publications. This table was adapted from 1.*

Ref	Catalyst	T (°C)	Plasma power (W)	H_2:N_2 ratio	EC (MJ/mol)	NH_3 yield (%)	NH_3 production rate (mg/h)
2	Ru/Al_2O_3	20	127	3:1	244	2.4	16
3	Cu	n/a*	n/a	1:1	19	1.4	71
4	DLC-coated Al_2O_3	160	70	3:1	350	n/a	12
5	PZT	60	n/a	3:1	94	7	34
6	Ru-Cs-K-Ba/ /Si-MCM-41	150	n/a	1:1	36	<0.1	n/a
7	RuO-MgO/Al_2O_3	300	4	1:4	2	<0.1	113
8	Ni/SiO_2 + $BaTiO_3$	140	87	3:1	81	12.0	32
9	Au	n/a	100	1:1	79	2.5	77
10	Co/Al_2O_3	200	10	2:1	36	1.0	17
11	Ni/Al_2O_3	35	10	2:1	56	0.7	10
12	Co/Al_2O_3	200	10	1:3	102	0.1	6
13	Ru/Al_2O_3	118	38	1:2	32	1.1	76
14	Ru/MgO	200	26	1:2	47	0.1	25
15	alkaline Al_2O_3	>105	24	3:1	9	<0.1	159
16	Rh/Al_2O_3	300	n/a	1:2	65	1.1	29
17	Ru/AC	n/a	13	3:1	85	0.5	10

* Not available: the data were missing, and the absence of the needed experimental data did not allow us to calculate the numerical values.

18	Ru-K/MgO	390	4	1:1	46	0.6	5
1	Co/Al_2O_3	<120	67	1:1	99	1.0	42
19	$Co-Ni/Al_2O_3$	200	31	1:1	37	0.6	51
20	Ru/AC	110	9	1:1	96	0.3	6
21	Zeolite 4A	57	6.4	1:2	27	2.6	15
22	Ni/MCM-41	35	40	3:1	51	5.3	48
This work	$CoLa/Al_2O_3$	<120	51	1:1	77	0.9	41

S1 Non-dispersive infrared sensor (NDIR)

In this study a non-dispersive infrared sensor is used to determine the NH_3 concentration at the outlet of the DBD reactor. The NDIR was calibrated by measuring various concentrations of NH3 diluted with helium. Table 13 shows the gas concentrations that were measured by the NDIR (C_{shown}) versus the actual NH_3 concentration (C_{real}). Plotting these values, generates the calibration equation:

$$2.10^{-10}\, C_{shown}{}^3 - 3.10^{-6}\, C_{shown}{}^2 + 0.9033\, C_{shown} = C_{real}$$

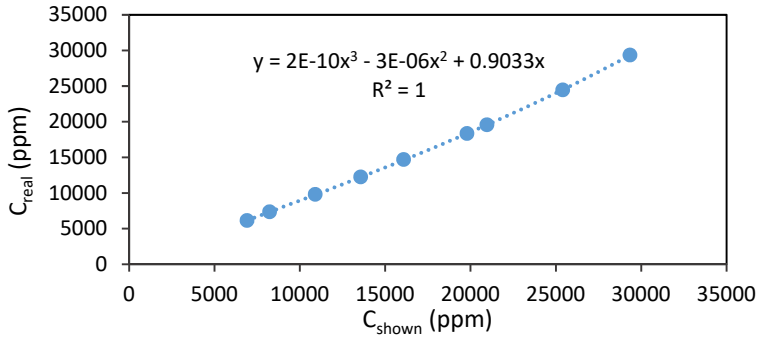

Figure S1: The measured NH_3 concentration versus the actual NH_3 concentration during the NDIR calibration.

S2 Raman spectroscopy

The Raman spectra were recorded on a Horiba XploRA Plus Raman spectrometer equipped with a diode-pumped solid-state laser of 532 nm and a power of 25 mW. The samples were measured with an acquisition time of 10 s, 10 accumulations and in a spectral range of 100-2000 cm^{-1}. The spectra were acquired in two different spots on two different beads, in order to verify the homogeneity of the catalysts.

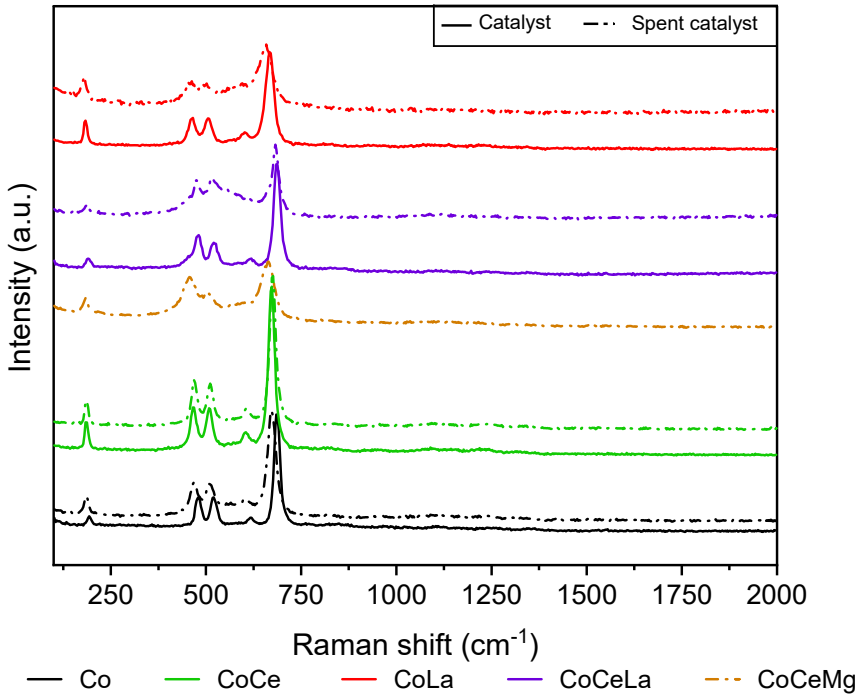

Figure S2: The Raman spectra of the fresh Co/Al_2O_3, $CoCe/Al_2O_3$, $CoCeLa/Al_2O_3$ and $CoLa/Al_2O_3$ catalysts.

All samples show Raman modes around similar shifts: ~190, ~477, ~520, ~622 and ~685 cm^{-1}. These modes are in good agreement with the values of pure Co_3O_4 spinel structure. For pure Co_3O_4 spinel structure with Co^{2+} and Co^{3+} located in the tetrahedral and octahedral sites, the space group theory predicts five Raman-active modes: A_{1g}, E_g and three F_{2g} modes.[31, 32] The A_{1g} band (~685 cm^{-1}) can be attributed to characteristics of the octahedral sites.[31-33] In addition, there is a general agreement that the E_g (~477 cm^{-1}) and F_{2g} (~190, ~520 and ~622 cm^{-1}) modes are related to the combined vibrations of the tetrahedral site and octahedral oxygen motions.[31, 33, 34] . Further, spent $CoCeMg/Al_2O_3$ and fresh and spent $CoCeLa/Al_2O_3$ all show a shoulder at ca. ~440 cm^{-1}, which could be attributed to the cubic fluorite structure of ceria (CeO_2) and/or to La_2O_3 in case of $CoCeLa/Al_2O_3$. The F_{2g} symmetry is the only Raman active mode of CeO_2[35] and is related to symmetrical stretch vibrations in the [CeO_8] cubic subunit of the CeO_2 structure.[36] In addition, fresh and spent $CoLa/Al_2O_3$ both show a shoulder around 445 cm^{-1} which could be assigned to La_2O_3. The E_g mode of La_2O_3 is correlated to the La-O stretching vibration, while the A_{1g} mode of La_2O_3 is ascribed to the La-O bending vibration.[37]

Table S2: The peak values of the Raman spectra of fresh Co/Al_2O_3, $CoCe/Al_2O_3$, $CoLa/Al_2O_3$, $CoCeLa/Al_2O_3$ and $CoCeMg/Al_2O_3$.

Sample	F_{2g} (Co_3O_4) (cm^{-1})			E_g (Co_3O_4) cm^{-1}	A_{1g} (Co_3O_4) (cm^{-1})	F_{2g} (CeO_2) (cm^{-1})	E_g (La_2O_3) (cm^{-1})	A_{1g} (La_2O_3) (cm^{-1})
Co/Al_2O_3	202	523	637	489	703	-	-	-
$CoCe/Al_2O_3$	180	523	605	480	680	-	-	-
$CoCeLa/Al_2O_3$	193	523	616	474	698	447	459	193
$CoLa/Al_2O_3$	196	523	604	444	665	-	447	196
$CoCeMg/Al_2O_3$	184	511	604	459	664	432	-	-

S3 SEM – EDX

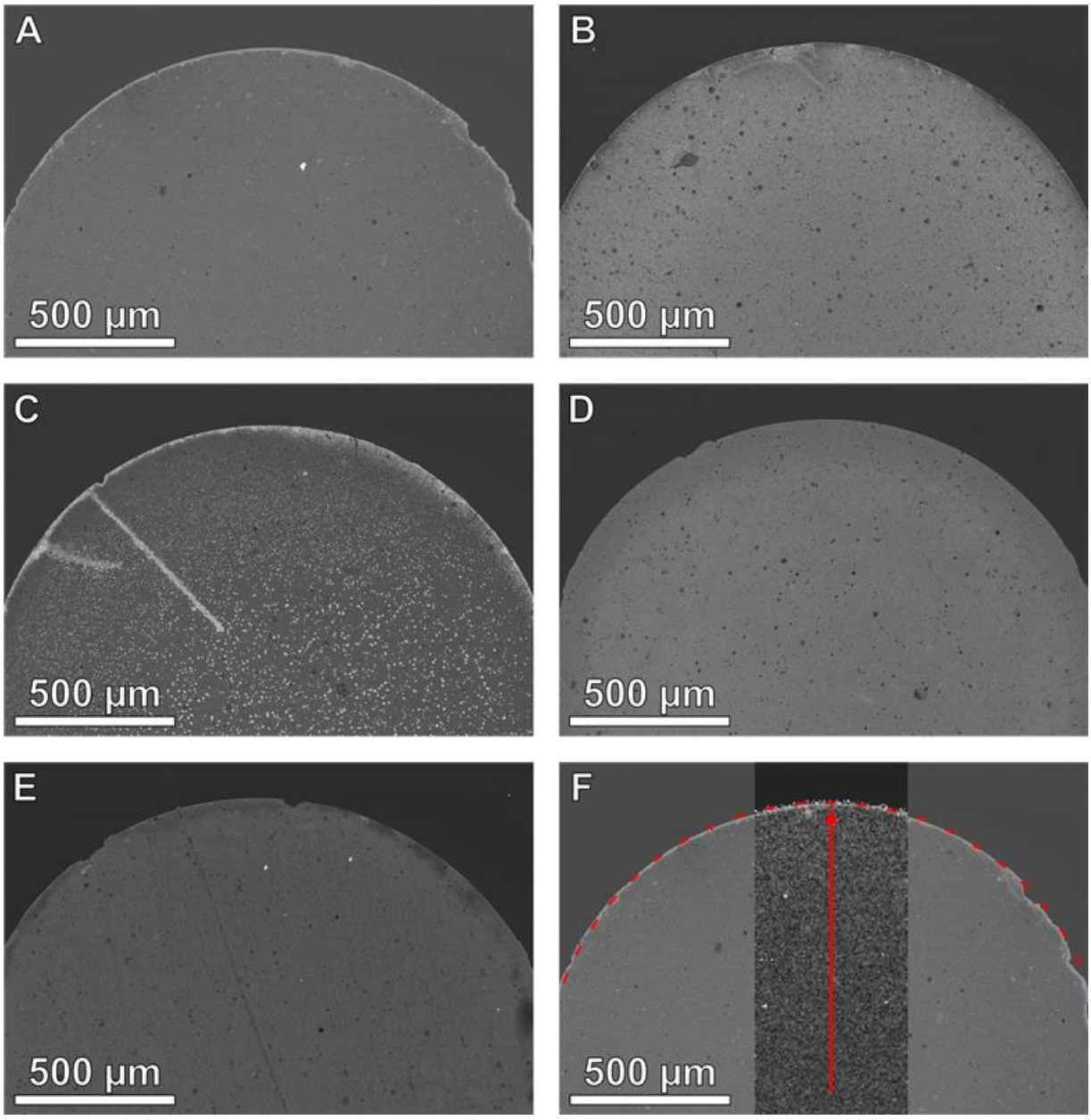

Figure S3: *SEM image of (A) Co/Al_2O_3, (B) $CoCe/Al_2O_3$, (C) $CoCeMg/Al_2O_3$, (D) $CoCeLa/Al_2O_3$ and (E) $CoLa/Al_2O_3$. (F) Shows the elemental EDX map for Co on top of image (A). The brighter pixels indicate a higher Co concentration. As is confirmed by the radial distribution, the Co sample displays a Co-rich area at the edge of the bead. As indicated in (F), a circle is fitted to the edge of the bead, so the distance from the center can be determined for every pixel, as indicated by the red arrow. This results in the radial distribution for the various elements.*

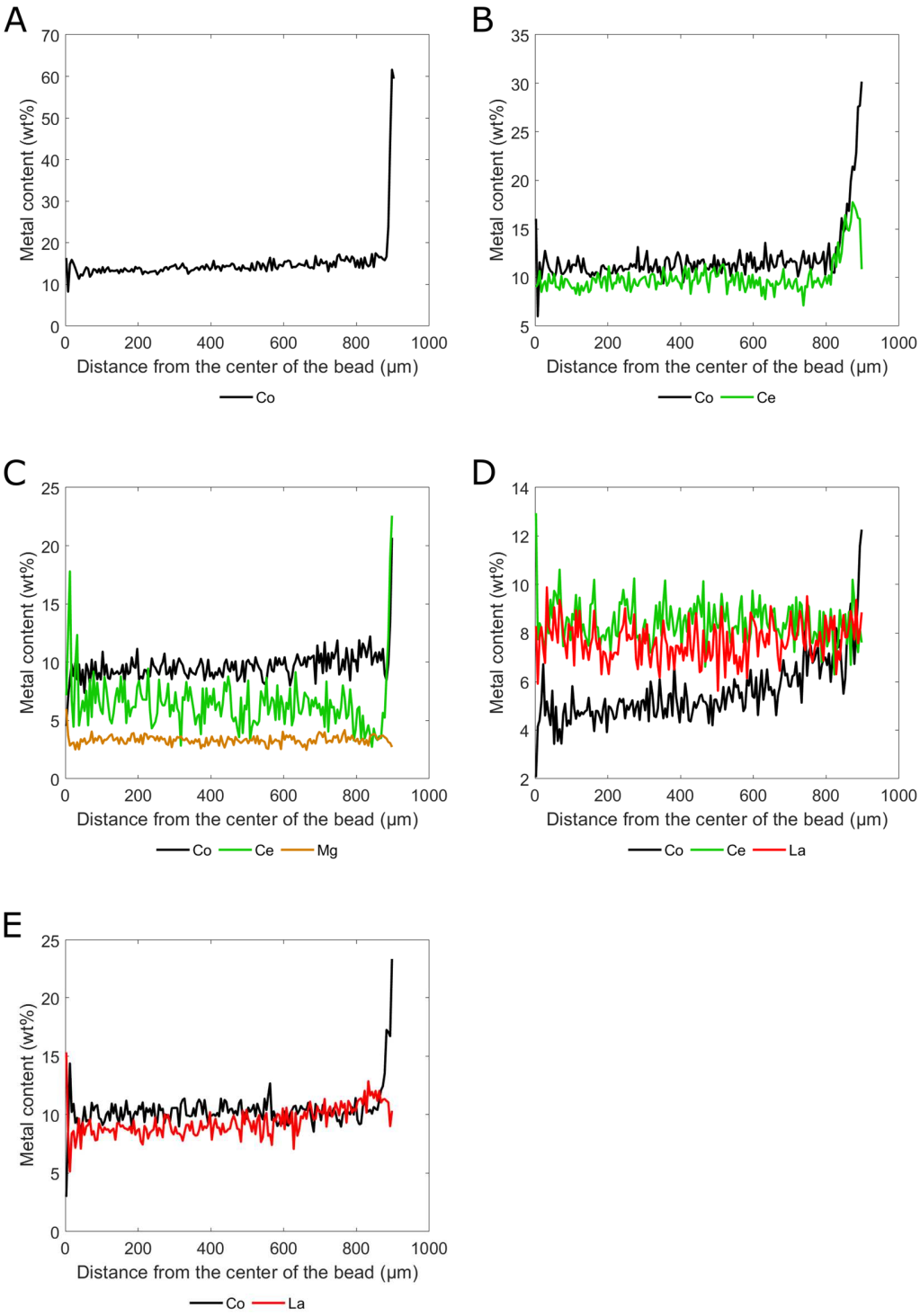

Figure S4: *The metal content as a function of the distance from the center of the bead for (A) Co/Al_2O_3, (B) CoCe/Al_2O_3, (C) CoCeMg/Al_2O_3, (D) CoCeLa/Al_2O_3 and (E) CoLa/Al_2O_3. From this plot it is clear that most of the metals are present on the outermost micrometers of the bead, which is beneficial for the plasma-catalytic synthesis of NH_3, as more active sites will be exposed to the plasma. Furthermore, this can alter the conductivity of the packing material, which affects the plasma discharge.*

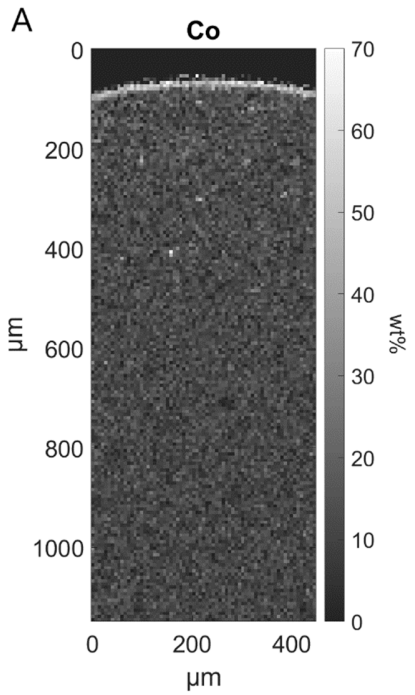

Figure S5: EDX map of the cross-section of a Co/Al_2O_3 bead.

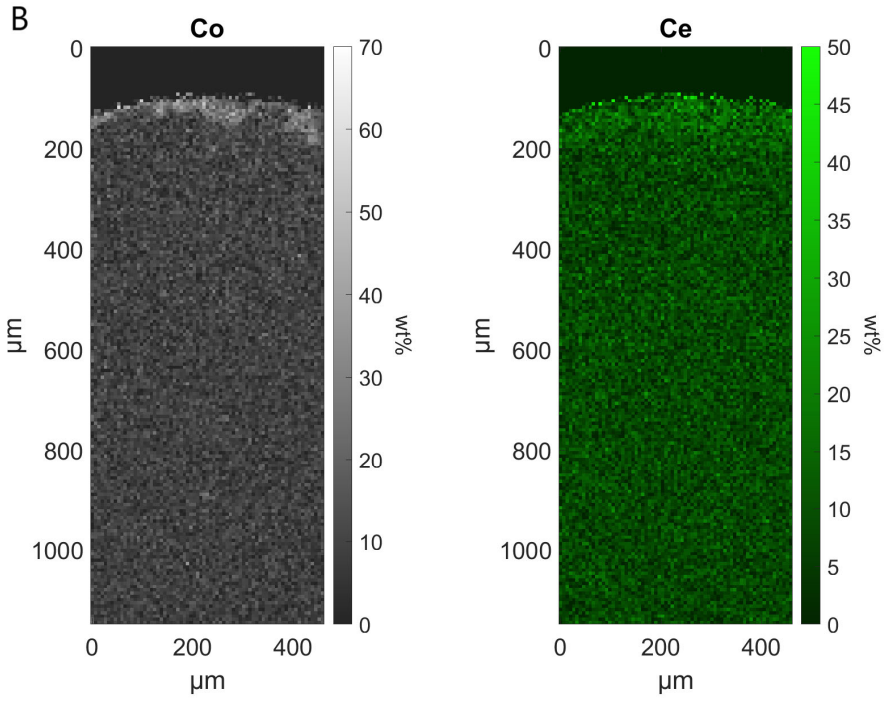

Figure S6: EDX map of the cross-section of a $CoCe/Al_2O_3$ bead.

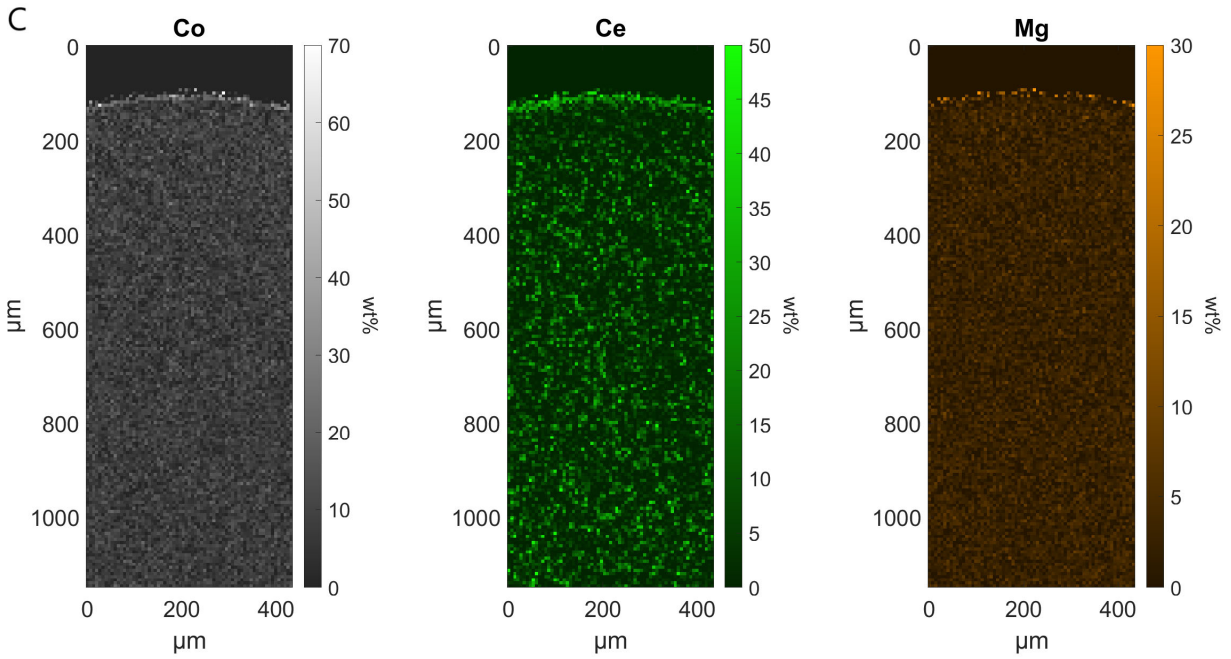

Figure S7: EDX map of the cross-section of a CoCeMg/Al_2O_3 bead.

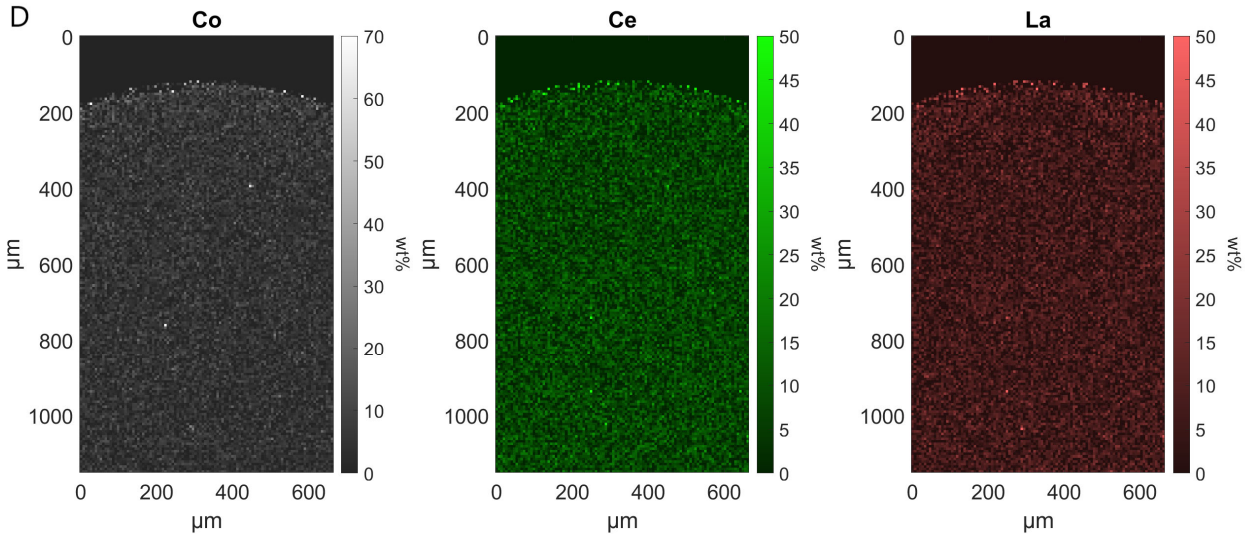

Figure S8: EDX map of the cross-section of a CoCeLa/Al_2O_3 bead.

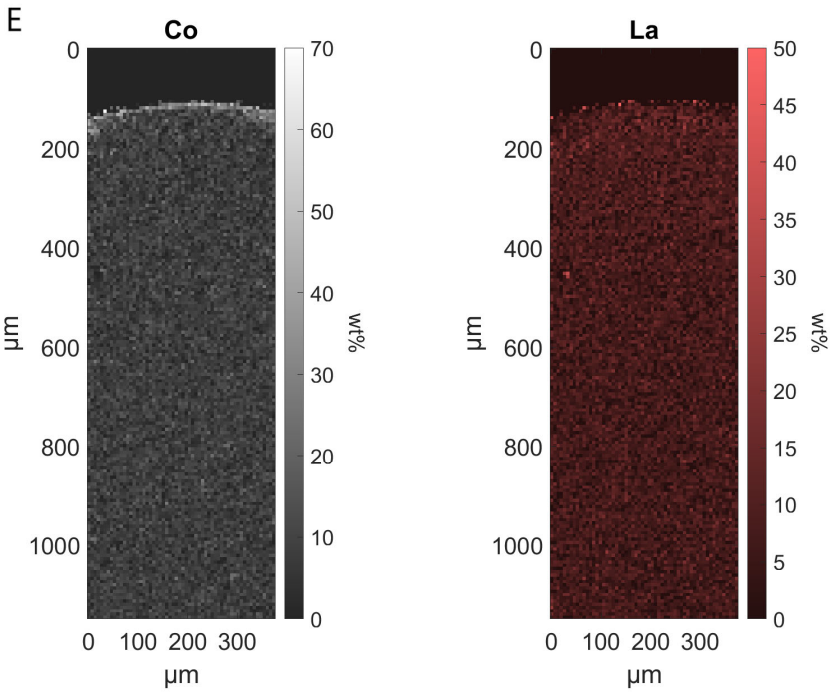

Figure S9: EDX map of the cross-section of a CoLa/Al_2O_3 bead.

S4 N_2 sorption

All the isotherms can be classified as type IV(a) in the IUPAC classification of physisorption isotherms, which are typical for mesoporous materials.[38]

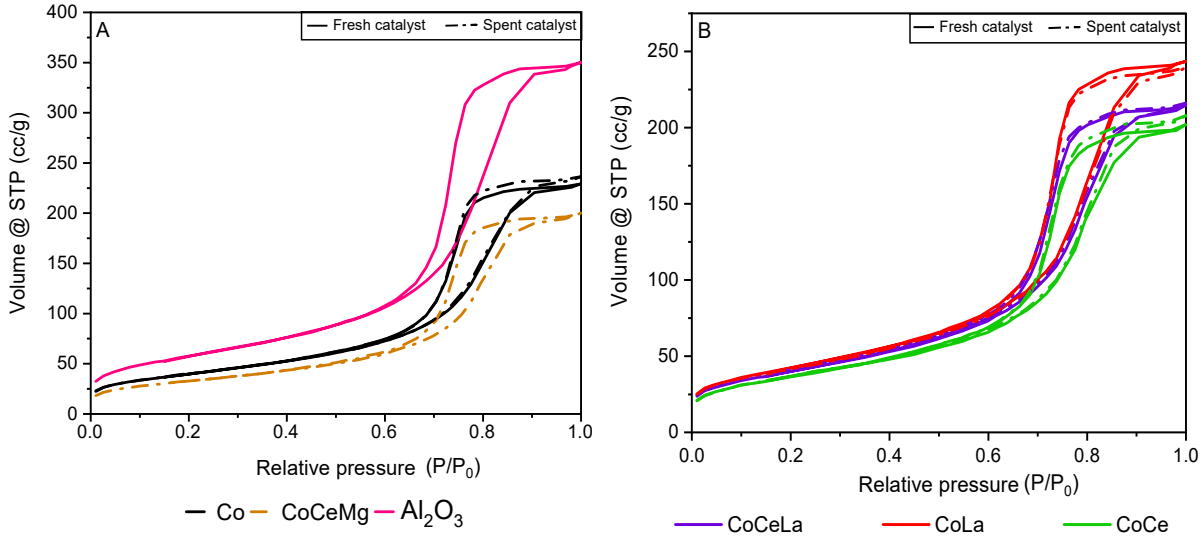

Figure S10: The physisorption isotherms of fresh and/or spent catalysts and pristine Al_2O_3.

S5 Plasma-catalytic performance

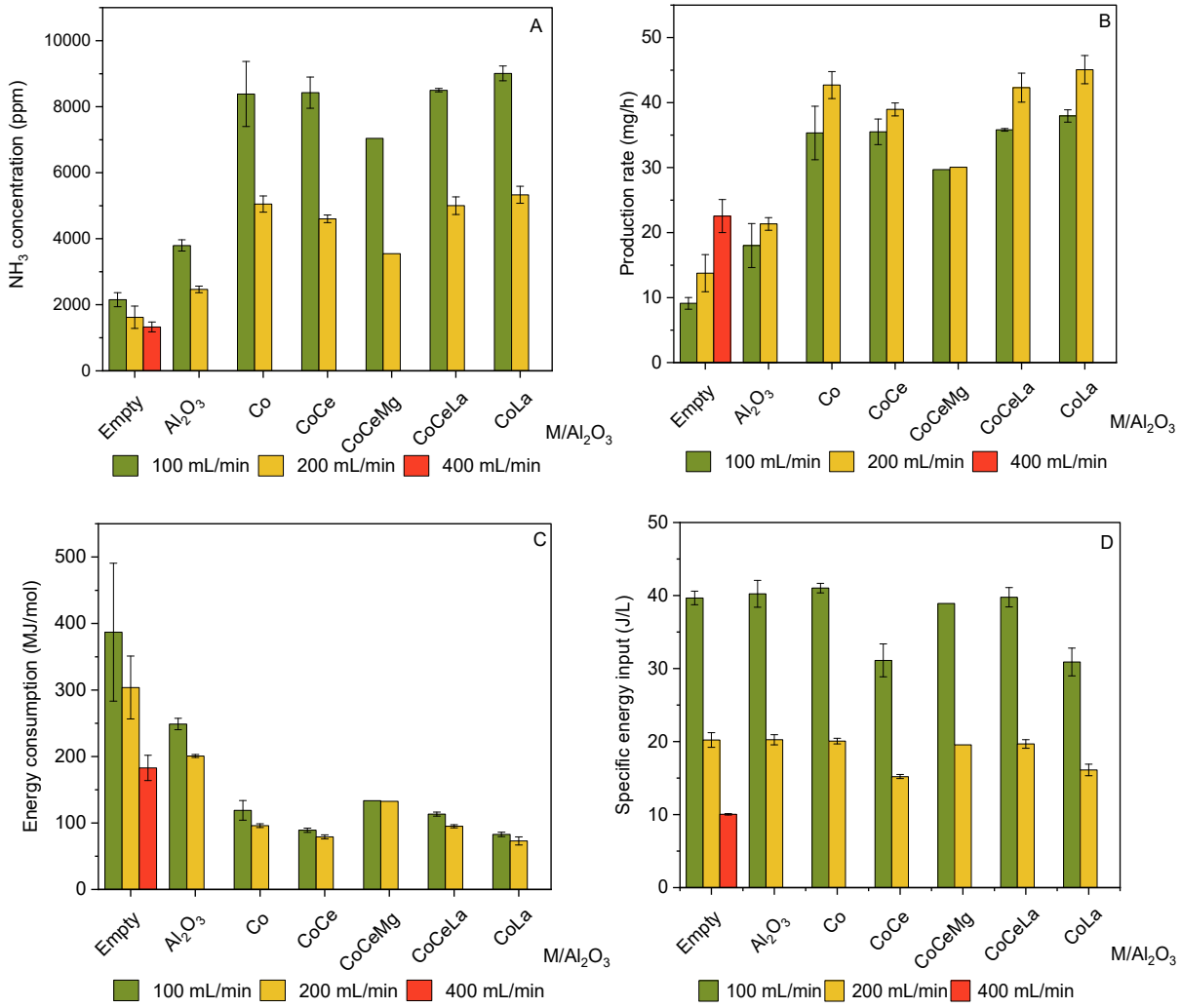

***Figure S11**: (A) NH_3 concentration, (B) production rate, (C) energy consumption and (D) specific energy input as a function of the gas flow rate for an empty reactor and a reactor packed with Al_2O_3 and the Co-based catalysts at a 1:1 H_2:N_2 ratio.*

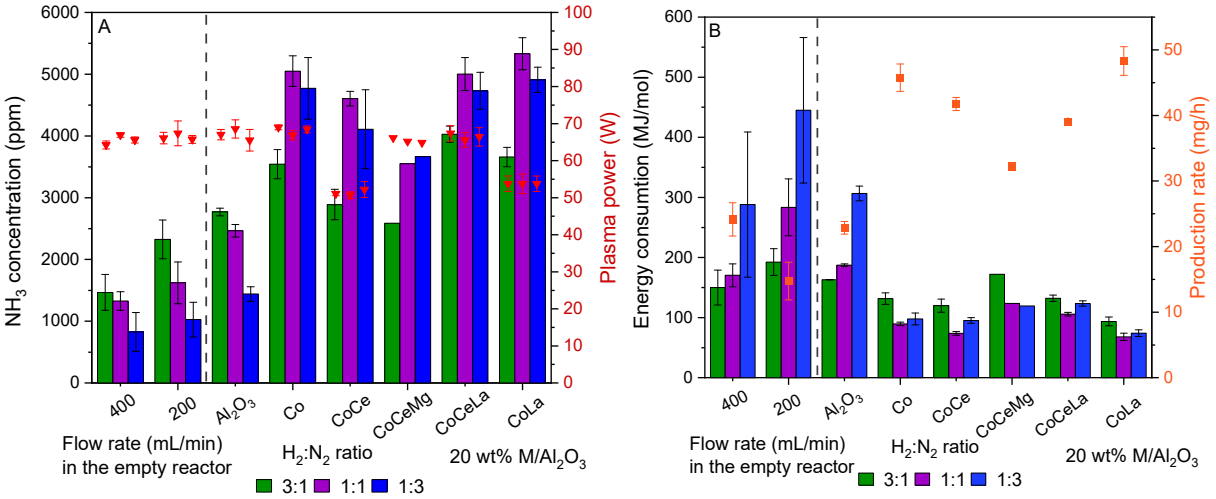

Figure S12: *(A) NH_3 concentration and power, and (B) energy consumption and production rate, for an empty DBD reactor, and a DBD reactor packed with Al_2O_3, Co/Al_2O_3, $CoCe/Al_2O_3$, $CoCeMg/Al_2O_3$, $CoCeLa/Al_2O_3$ and $CoLa/Al_2O_3$ catalysts, operating at 200 mL/min and at three different H_2:N_2 ratios. The empty reactor was used with two different feed gas flow rates: 400 and 200 mL/min, to obtain the same residence time and same mass flow rate, respectively, as the packed reactor.*

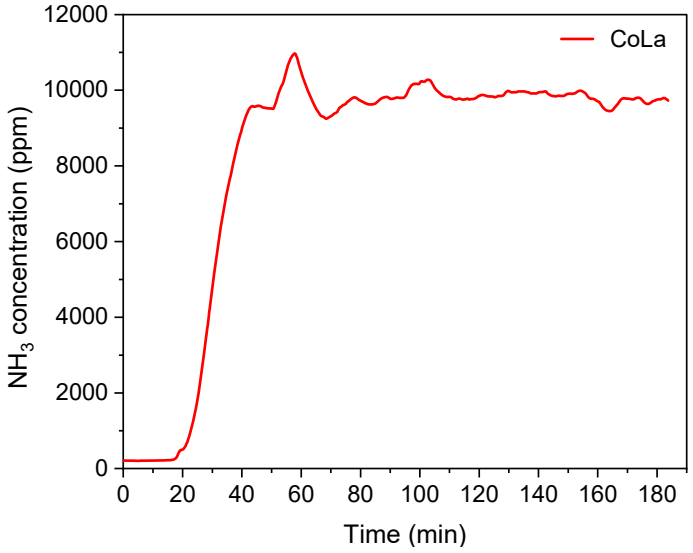

Figure S13: *The NH_3 concentration as a function of time for the reaction using $CoLa/Al_2O_3$ as packed catalysts.*

References

(1) Gorbanev, Y.; Engelmann, Y.; van't Veer, K.; Vlasov, E.; Ndayirinde, C.; Yi, Y.; Bals, S.; Bogaerts, A. Al2O3-Supported Transition Metals for Plasma-Catalytic NH3 Synthesis in a DBD Plasma: Metal Activity and Insights into Mechanisms. *Catalysts* **2021**, *11* (10). DOI: 10.3390/catal11101230.

(2) Mizushima, T.; Matsumoto, K.; Sugoh, J.-i.; Ohkita, H.; Kakuta, N. Tubular membrane-like catalyst for reactor with dielectric-barrier-discharge plasma and its performance in ammonia synthesis. *Appl. Catal.* **2004**, *265* (1), 53-59. DOI: 10.1016/j.apcata.2004.01.002.

(3) Aihara, K.; Akiyama, M.; Deguchi, T.; Tanaka, M.; Hagiwara, R.; Iwamoto, M. Remarkable catalysis of a wool-like copper electrode for NH 3 synthesis from N 2 and H 2 in non-thermal atmospheric plasma. *Chem. Commun.* **2016**, *52* (93), 13560-13563. DOI: 10.1039/C6CC06752B.

(4) Hong, J.; Aramesh, M.; Shimoni, O.; Seo, D. H.; Yick, S.; Greig, A.; Charles, C.; Prawer, S.; Murphy, A. B. Plasma catalytic synthesis of ammonia using functionalized-carbon coatings in an atmospheric-pressure non-equilibrium discharge. *Plasma Chem. Plasma Process.* **2016**, *36* (4), 917-940. DOI: 10.1007/s11090-016-9711-8.

(5) Gómez-Ramírez, A.; Montoro-Damas, A. M.; Cotrino, J.; Lambert, R. M.; González-Elipe, A. R. About the enhancement of chemical yield during the atmospheric plasma synthesis of ammonia in a ferroelectric packed bed reactor. *Plasma Process Polym* **2017**, *14* (6), 1600081. DOI: 10.1002/ppap.201600081.

(6) Peng, P.; Cheng, Y.; Hatzenbeller, R.; Addy, M.; Zhou, N.; Schiappacasse, C.; Chen, D.; Zhang, Y.; Anderson, E.; Liu, Y. Ru-based multifunctional mesoporous catalyst for low-pressure and non-thermal plasma synthesis of ammonia. *Int. J. Hydrogen Energy* **2017**, *42* (30), 19056-19066. DOI: 10.1016/j.ijhydene.2017.06.118.

(7) Kim, H. H.; Teramoto, Y.; Ogata, A.; Takagi, H.; Nanba, T. Atmospheric-pressure nonthermal plasma synthesis of ammonia over ruthenium catalysts. *Plasma Process Polym* **2017**, *14* (6), 1600157. DOI: 10.1002/ppap.201600157.

(8) Akay, G.; Zhang, K. Process intensification in ammonia synthesis using novel coassembled supported microporous catalysts promoted by nonthermal plasma. *Ind. Eng. Chem. Res.* **2017**, *56* (2), 457-468. DOI: 10.1021/acs.iecr.6b02053.

(9) Iwamoto, M.; Akiyama, M.; Aihara, K.; Deguchi, T. Ammonia synthesis on wool-like Au, Pt, Pd, Ag, or Cu electrode catalysts in nonthermal atmospheric-pressure plasma of N2 and H2. *ACS Catal.* **2017**, *7* (10), 6924-6929. DOI: 10.1021/acscatal.7b01624.

(10) Mehta, P.; Barboun, P.; Herrera, F. A.; Kim, J.; Rumbach, P.; Go, D. B.; Hicks, J. C.; Schneider, W. F. Overcoming ammonia synthesis scaling relations with plasma-enabled catalysis. *Nat. Catal.* **2018**, *1* (4), 269-275. DOI: 10.1038/s41929-018-0045-1.

(11) Wang, Y.; Craven, M.; Yu, X.; Ding, J.; Bryant, P.; Huang, J.; Tu, X. Plasma-Enhanced Catalytic Synthesis of Ammonia over a Ni/Al2O3 Catalyst at Near-Room Temperature: Insights into the Importance of the Catalyst Surface on the Reaction Mechanism. *ACS Catal.* **2019**, *9* (12), 10780-10793. DOI: 10.1021/acscatal.9b02538.

(12) Barboun, P.; Mehta, P.; Herrera, F. A.; Go, D. B.; Schneider, W. F.; Hicks, J. C. Distinguishing Plasma Contributions to Catalyst Performance in Plasma-Assisted Ammonia Synthesis. *ACS Sustain. Chem. Eng.* **2019**, *7* (9), 8621-8630. DOI: 10.1021/acssuschemeng.9b00406.

(13) Li, S.; van Raak, T.; Gallucci, F. Investigating the operation parameters for ammonia synthesis in dielectric barrier discharge reactors. *J. Phys. D: Appl. Phys.* **2020**, *53* (1). DOI: 10.1088/1361-6463/ab4b37.

(14) Xie, Q.; Zhuge, S.; Song, X.; Lu, M.; Yu, F.; Ruan, R.; Nie, Y. Non-thermal atmospheric plasma synthesis of ammonia in a DBD reactor packed with various catalysts. *J. Phys. D: Appl. Phys.* **2019**, *53* (6), 064002. DOI: 10.1088/1361-6463/ab57e5.

(15) Zhu, X.; Hu, X.; Wu, X.; Cai, Y.; Zhang, H.; Tu, X. Ammonia synthesis over γ-Al2O3 pellets in a packed-bed dielectric barrier discharge reactor. *J. Phys. D: Appl. Phys.* **2020**, *53* (16), 164002. DOI: 10.1088/1361-6463/ab6cd1.
(16) Patil, B. S.; Cherkasov, N.; Srinath, N. V.; Lang, J.; Ibhadon, A. O.; Wang, Q.; Hessel, V. The role of heterogeneous catalysts in the plasma-catalytic ammonia synthesis. *Catal. Today* **2021**, *362*, 2-10. DOI: 10.1016/j.cattod.2020.06.074.
(17) Hu, X.; Zhu, X.; Wu, X.; Cai, Y.; Tu, X. Plasma-enhanced NH3 synthesis over activated carbon-based catalysts: Effect of active metal phase. *Plasma Process Polym* **2020**, *17* (12), 2000072. DOI: 10.1002/ppap.202000072.
(18) Rouwenhorst, K. H.; Burbach, H. G.; Vogel, D. W.; Paulí, J. N.; Geerdink, B.; Lefferts, L. Plasma-catalytic ammonia synthesis beyond thermal equilibrium on Ru-based catalysts in non-thermal plasma. *Catal. Sci. Technol.* **2021**. DOI: 10.1039/D0CY02189J.
(19) Liu, Y.; Wang, C.-W.; Xu, X.-F.; Liu, B.-W.; Zhang, G.-M.; Liu, Z.-W.; Chen, Q.; Zhang, H.-B. Synergistic Effect of Co–Ni Bimetal on Plasma Catalytic Ammonia Synthesis. *Plasma Chem. Plasma Process.* **2022**, 1-16. DOI: 10.1007/s11090-021-10223-1.
(20) Zhu, X.; Liu, J.; Hu, X.; Zhou, Z.; Li, X.; Wang, W.; Wu, R.; Tu, X. Plasma-catalytic synthesis of ammonia over Ru-based catalysts: Insights into the support effect. *Journal of the Energy Institute* **2022**. DOI: 10.1016/j.joei.2022.02.014.
(21) Rouwenhorst, K. H.; Mani, S.; Lefferts, L. Improving the energy yield of plasma-based ammonia synthesis with in situ adsorption. *ACS Sustain. Chem. Eng.* **2022**, *10* (6), 1994-2000. DOI: 10.1021/acssuschemeng.1c08467.
(22) Wang, Y.; Yang, W.; Xu, S.; Zhao, S.; Chen, G.; Weidenkaff, A.; Hardacre, C.; Fan, X.; Huang, J.; Tu, X. Shielding protection by mesoporous catalysts for improving plasma-catalytic ambient ammonia synthesis. *Journal of the American Chemical Society* **2022**. DOI: 10.1021/jacs.2c01950.
(23) Zhang, L.; Zhao, X.; Ma, W.; Wu, M.; Qian, N.; Lu, W. Novel three-dimensional Co 3 O 4 dendritic superstructures: hydrothermal synthesis, formation mechanism and magnetic properties. *CrystEngComm* **2013**, *15* (7), 1389-1396. DOI: 10.1039/C2CE26374B.
(24) Duan, X.; Pan, M.; Yu, F.; Yuan, D. Synthesis, structure and optical properties of CoAl2O4 spinel nanocrystals. *J. Alloys Compd.* **2011**, *509* (3), 1079-1083. DOI: 10.1016/j.jallcom.2010.09.199.
(25) Srisawad, N.; Chaitree, W.; Mekasuwandumrong, O.; Praserthdam, P.; Panpranot, J. Formation of CoAl2O4Nanoparticles via Low-Temperature Solid-State Reaction of Fine Gibbsite and Cobalt Precursor. *Journal of Nanomaterials* **2012**, *2012*, 1-8. DOI: 10.1155/2012/108369.
(26) Kim, K. S.; Park, Y. J. Catalytic properties of Co3O4 nanoparticles for rechargeable Li/air batteries. *Nanoscale Research Letters* **2012**, *7* (1). DOI: 10.1186/1556-276x-7-47.
(27) Kanwal, F.; Batool, A.; Adnan, M.; Naseem, S. The effect of molecular structure, band gap energy and morphology on the dc electrical conductivity of polyaniline/aluminium oxide composites. *Mater. Res. Innovations* **2015**, *19* (sup8), S8-354-S358-358. DOI: 10.1179/1432891715Z.0000000001688.
(28) Gurram, V. R. B.; Enumula, S. S.; Mutyala, S.; Pochamoni, R.; Prasad, P. S. S.; Burri, D. R.; Kamaraju, S. R. R. The advantage of ceria loading over V2O5/Al2O3 catalyst for vapor phase oxidative dehydrogenation of ethylbenzene to styrene using CO2 as a soft oxidant. *Applied Petrochemical Research* **2016**, *6* (4), 427-437. DOI: 10.1007/s13203-016-0163-0.
(29) Xue, S.-F.; Wu, W.-Y.; Bian, X.; Wang, Z.-F.; Wu, Y.-F. Facile preparation of CeO2 microspheres with high surface area by ultrasonic spray pyrolysis. *Green Processing and Synthesis* **2018**, *7* (3), 241-247. DOI: 10.1515/gps-2017-0041.
(30) Wang, J.; Li, Z.; Zhang, S.; Yan, S.; Cao, B.; Wang, Z.; Fu, Y. Enhanced NH3 gas-sensing performance of silica modified CeO2 nanostructure based sensors. *Sensors and Actuators B: Chemical* **2018**, *255*, 862-870. DOI: 10.1016/j.snb.2017.08.149.

(31) Rashad, M.; Rüsing, M.; Berth, G.; Lischka, K.; Pawlis, A. CuO and Co3O4 nanoparticles: synthesis, characterizations, and Raman spectroscopy. *Journal of Nanomaterials* **2013**, *2013*. DOI: 10.1155/2013/714853.
(32) Deng, S.; Chen, N.; Deng, D.; Li, Y.; Xing, X.; Wang, Y. Meso-and macroporous coral-like Co3O4 for VOCs gas sensor. *Ceram. Int.* **2015**, *41* (9), 11004-11012. DOI: 10.1016/j.ceramint.2015.05.045.
(33) Diallo, A.; Beye, A.; Doyle, T. B.; Park, E.; Maaza, M. Green synthesis of Co3O4 nanoparticles via Aspalathus linearis: physical properties. *Green Chemistry Letters and Reviews* **2015**, *8* (3-4), 30-36. DOI: 10.1080/17518253.2015.1082646.
(34) Rivas-Murias, B.; Salgueiriño, V. Thermodynamic CoO–Co3O4 crossover using Raman spectroscopy in magnetic octahedron-shaped nanocrystals. *Journal of Raman Spectroscopy* **2017**, *48* (6), 837-841. DOI: 10.1002/jrs.5129.
(35) Pushkarev, V. V.; Kovalchuk, V. I.; d'Itri, J. L. Probing defect sites on the CeO2 surface with dioxygen. *The Journal of Physical Chemistry B* **2004**, *108* (17), 5341-5348. DOI: 10.1021/jp0311254.
(36) Loridant, S. Raman spectroscopy as a powerful tool to characterize ceria-based catalysts. *Catal. Today* **2020**. DOI: 10.1016/j.cattod.2020.03.044.
(37) Wang, N.; Liu, J.; Gu, W.; Song, Y.; Wang, F. Toward synergy of carbon and La2O3 in their hybrid as an efficient catalyst for the oxygen reduction reaction. *RSC Advances* **2016**, *6* (81), 77786-77795. DOI: 10.1039/c6ra17104d.
(38) Thommes, M.; Kaneko, K.; Neimark, A. V.; Olivier, J. P.; Rodriguez-Reinoso, F.; Rouquerol, J.; Sing, K. S. Physisorption of gases, with special reference to the evaluation of surface area and pore size distribution (IUPAC Technical Report). *Pure Appl. Chem.* **2015**, *87* (9-10), 1051-1069. DOI: 10.1515/pac-2014-1117.